



ELSEVIER

Dynamics of Atmospheres and Oceans 32 (2000) 373–417

www.elsevier.com/locate/dynatmoce

dynamics
of atmospheres
and oceans

Modeled Sverdrup flow in the North Atlantic from 11 different wind stress climatologies

Tamara L. Townsend^{*}, Harley E. Hurlburt, Patrick J. Hogan

Naval Research Laboratory, Stennis Space Center, MS 39529-5004, USA

Received 12 August 1998; received in revised form 11 August 1999; accepted 12 January 2000

Abstract

In studies of large-scale ocean dynamics, often quoted values of Sverdrup transport are computed using the Hellerman–Rosenstein wind stress climatology. The Sverdrup solution varies, however, depending on the wind set used. We examine the differences in the large-scale upper ocean response to different surface momentum forcing fields for the North Atlantic Ocean by comparing the different Sverdrup interior/Munk western boundary layer solutions produced by a $1/16^\circ$ linear numerical ocean model forced by 11 different wind stress climatologies. Significant differences in the results underscore the importance of careful selection of a wind set for Sverdrup transport calculation and for driving nonlinear models. This high-resolution modeling approach to solving the linear wind-driven ocean circulation problem is a convenient way to discern details of the Sverdrup flow and Munk western boundary layers in areas of complicated geometry such as the Caribbean and Bahamas. In addition, the linear solutions from a large number of wind sets provide a well-understood baseline oceanic response to wind stress forcing and thus, (1) insight into the dynamics of observed circulation features, by themselves and in conjunction with nonlinear models, and (2) insight into nonlinear model sensitivity to the choice of wind-forcing product.

The wind stress products are evaluated and insight into the linear dynamics of specific ocean features is obtained by examining wind stress curl patterns in relation to the corresponding high-resolution linear solutions in conjunction with observational knowledge of the ocean circulation. In the Sverdrup/Munk solutions, the Gulf Stream pathway consists of two branches. One separates from the coast at the observed separation point, but penetrates due east in an unrealistic manner. The other, which overshoots the separation point at Cape Hatteras and continues to flow northward along the continental boundary, is required to balance the Sverdrup interior transport. A

^{*} Corresponding author.

E-mail address: townsend@nrlssc.navy.mil (T.L. Townsend).

similar depiction of the Gulf Stream is commonly seen in the mean flow of nonlinear, eddy-resolving basin-scale models of the North Atlantic Ocean. An $O(1)$ change from linear dynamics is required for realistic simulation of the Gulf Stream pathway. Nine of the eleven Sverdrup solutions have a C-shaped subtropical gyre, similar to what is seen in dynamic height contours derived from observations. Three mechanisms are identified that can contribute to this pattern in the Sverdrup transport contours. Along 27°N , several wind sets drive realistic total western boundary current transport (within 10% of observed) when a 14 Sv global thermohaline contribution is added (COADS, ECMWF 10 m re-analysis and operational, Hellerman–Rosenstein and National Centers for Environmental Prediction (NCEP) surface stress re-analysis), a few drive transport that is substantially too high (ECMWF 1000 mb re-analysis and operational and Isemer–Hasse) and Fleet Numerical Meteorology and Oceanography Center (FNMOC) surface stresses give linear transport that is slightly weaker than observed. However, higher order dynamics are required to explain the partitioning of this transport between the Florida Straits and just east of the Bahamas (minimal in the linear solutions vs. 5 Sv observed east of the Bahamas). Part of the Azores Current transport is explained by Sverdrup dynamics. So are the basic path of the North Atlantic Current (NAC) and the circulation features within the Intra-Americas Sea (IAS), when a linear rendition of the northward upper ocean return flow of the global thermohaline circulation is added in the form of a Munk western boundary layer. © 2000 Elsevier Science B.V. All rights reserved.

Keywords: Sverdrup flow; Wind stress; North Atlantic

1. Introduction

Since surface momentum flux due to wind stress forcing is the primary driving mechanism for upper ocean currents, it is useful, given a wind stress climatology, to compute an estimate of the mean large-scale upper ocean response using the lowest order approximation to the relevant dynamics. Sverdrup (1947) first demonstrated a balance between wind stress curl and meridional planetary vorticity advection in the equatorial Pacific. Stommel (1948) and Munk (1950) closed the gyre circulation with western boundary currents within a viscous boundary layer, allowing estimation of the large-scale upper ocean circulation from equatorial regions to high latitudes based on low order ocean dynamics and the distribution of the wind stress curl over the ocean. Godfrey (1989) extended this capability to include islands.

This study is motivated by the widespread use of the Hellerman and Rosenstein (1983) (HR hereafter) wind stress climatology in calculating Sverdrup transports (Roemmich and Wunsch, 1985; Wunsch and Roemmich, 1985; Lee et al., 1990, 1996; Fratantoni et al., 2000) and the fact that other global wind stress climatologies have been developed since the introduction of the HR climatology. The choice of wind stress climatology can be significant when studying large-scale ocean dynamics since different wind stress products yield substantial differences in flow patterns, transport magnitudes, and distribution of flow through island passages. Here, we compare the Atlantic Sverdrup flow patterns resulting from 11 different wind stress climatologies.

Rather than using the analytical methods of Sverdrup (1947) and Munk (1950) separately and applying Godfrey's (1989) technique in the vicinity of islands, we

compute the Sverdrup solution everywhere using a $1/16^\circ$ linear numerical ocean model. In addition to obtaining a Sverdrup interior with the large-scale gyres closed by a Munk western boundary layer, it is a convenient way to handle islands in order to obtain quantitative passage transports instead of estimates. The linear wind-driven solutions are essentially the same as Munk (1950) with a Sverdrup (1947) interior calculated using realistic wind forcing and model geometry, including islands, except that horizontal friction is applied everywhere and, especially in the tropics, the model sea surface height includes the tilt due to pile up of the water by the predominantly zonal wind stress. However, the latter has no effect on the transport streamfunction. In addition, the use of a high-resolution numerical model leads to more accurate descriptions of the large-scale wind-driven ocean response than seen in previous studies (e.g., Leetmaa and Bunker, 1978; Leetmaa et al., 1977; Roemmich and Wunsch, 1985; Schmitz et al., 1992; Fratantoni et al., 2000). This is because (1) the lower eddy viscosity leads to things like sharper currents, and (2) the complicated coastline geometry, which affects the passage transports, is better resolved. With an appropriate choice of layer thickness and stratification, it also offers the opportunity to examine the linear time-dependent response to wind forcing (which is generally not in Sverdrup balance). The focus here, however, is on the Sverdrup balance between wind stress curl and mass transport, which does not hold for any given month or season outside the equatorial region. Therefore, all results presented are annual means.

Using a linear ocean model rather than solving the Sverdrup equation directly also presents another opportunity. Since a linear model includes only the lowest order dynamics of the ocean circulation, these simulations provide a baseline comparison of ocean model response to different wind forcing products and insight into the dynamics of more complex numerical simulations. They provide a benchmark for other simulations which have added features like nonlinearity, bottom topography, multiple vertical modes, flow instabilities, thermal forcing and vertical mixing. All 11 wind stress climatologies used in this study are available for forcing numerical ocean models. Most are used to some extent by the ocean modeling community and some are quite commonly used. There are two points of emphasis in this study. First, since the linear dynamics are well understood and there are no vagaries of nonlinearities, the Sverdrup solutions from a large number of wind sets can provide substantial insight into the dynamics of observed and simulated large-scale circulation features. Second, in conjunction with what is known about the large-scale North Atlantic circulation, the linear solutions provide an oceanographic means to evaluate wind stress products by appropriate model–data comparisons and by examining wind stress curl patterns in relation to the corresponding high-resolution linear solutions which have detailed deep basin boundaries and islands.

In addition to the Sverdrup/Munk flow resulting from various wind stress climatologies, we consider how this flow is altered by the Atlantic meridional overturning cell (MOC). The MOC is part of the global thermohaline circulation and has been shown to play a significant role in the circulation of the North Atlantic (Schmitz and Richardson, 1991 (SR91, hereafter); Fratantoni et al., 1995, 2000). Driven by deep water formation in the far North Atlantic, this component of the North Atlantic circulation includes southward-flowing North Atlantic Deep Water (NADW) and an upper ocean return

flow. We examine the contribution of the upper portion of the MOC to the upper North Atlantic circulation by adding a linear version of this MOC component (computed with the same $1/16^\circ$ numerical ocean model) to the linear solution produced by the HR monthly mean wind stress climatology.

The numerical model is described in Section 2 and the wind stress climatologies are presented and compared in Section 3. In Section 4, we compare the transports and transport pathways of Sverdrup interior flow and Munk western boundary currents in the North Atlantic Ocean, Caribbean Sea, and Gulf of Mexico resulting from these wind stress forcing sets. This includes comparisons to some of the observed large-scale features and discussions of the lowest-order dynamics of these features. In Section 5, we present a linear rendition of the upper (northward) portion of the MOC and its impact on the North Atlantic wind-driven circulation. A summary of the study is presented in Section 6 along with conclusions regarding the wind stress climatologies, the inference of the large-scale ocean response using the Sverdrup (1947) relation, and the implications in choosing wind forcing data sets for ocean circulation models.

2. The ocean model

The linear numerical simulations were performed using the NRL Layered Ocean Model (NLOM), a nonlinear free surface model but one which can easily be configured for linear simulations. The model is a primitive equation, layered formulation where the model equations are vertically integrated through each layer and the interfaces between each layer are isopycnal. It is a descendant of the model by Hurlburt and Thompson (1980) with expanded capability (Wallcraft, 1991; Wallcraft and Moore, 1997) including spherical coordinates. The model boundary conditions are kinematic and no slip. Although thermodynamic versions of the model exist (Metzger et al., 1992; Heburn, 1994; Metzger and Hurlburt, 1996), purely hydrodynamic versions are used here. Also, no cross-isopycnal mixing occurs in the simulations presented here. For other hydrodynamic as well as thermodynamic configurations of the model, however, ventilation of the isopycnal surfaces, as described by Shriver and Hurlburt (1997), does occur, allowing closed vertical circulations within the model domain and shallow layers in a basin-scale model.

The investigation of Sverdrup flow resulting from various wind forcing fields requires only the determination of the total transport in the upper ocean. Sverdrup did not attempt to determine the distribution of velocity with depth in the upper ocean and he assumed no abyssal flow. The same transport streamfunction for the mean flow is obtained using a barotropic flat bottom model with negligible bottom stress. For the steady-state linear solutions, which have no diapycnal mixing or interfacial stress between the isopycnal layers, there is no driving mechanism for mean flow below the top layer. Therefore, it is sufficient to employ either a finite depth, flat bottom model, or a reduced gravity model with one active Lagrangian layer above an infinitely deep inert lower layer. The latter choice is made here. The full nonlinear model equations (Hurlburt and Hogan, 2000, this issue) were used. However, they reduce to the

following when the model is linearized by scaling the forcing by 0.001 so that the advective effects and interface deviations are small and nonlinearity is negligible.

$$\frac{\partial \vec{v}_1}{\partial t} + \hat{k} \times f \vec{v}_1 = - [g(\rho_2 - \rho_1)/\rho_0] \nabla h_1 + (\vec{\tau}_0 - \vec{\tau}_1)/(\rho_0 H_1) + A_H \nabla^2 \vec{v}_1$$

$$\frac{\partial h_1}{\partial t} + H_1 \nabla \cdot \vec{v}_1 = 0$$

where: \vec{v}_1 = layer 1 velocity; f = Coriolis parameter; g = acceleration due to gravity; ρ_0 = constant reference density; ρ_1 = layer 1 density, constant in space and time; ρ_2 = layer 2 density, constant in space and time; h_1 = layer 1 thickness; H_1 = layer 1 thickness at rest; $\vec{\tau}_0$ = wind stress; $\vec{\tau}_1 = 0$; A_H = coefficient of horizontal eddy viscosity.

The model equations are integrated on a C-grid (Mesinger and Arakawa, 1976) using an explicit in time numerical scheme for the reduced gravity experiments used in this study. See Hurlburt et al. (1996), Shriver and Hurlburt (1997), and Hurlburt and Hogan (2000, this issue) as examples of applications which use the more general features of the nonlinear NLOM.

The basin-scale model of the North Atlantic Ocean extends from 30°S to 65°N (Fig. 1a) and includes the Gulf of Mexico and Caribbean Sea, both of which lie in the pathway of the Gulf Stream System. These two semi-enclosed seas along with the adjacent waters of the North Atlantic comprise the Intra-Americas Sea (IAS, Fig. 1b). Simulations with horizontal grid resolution of 1/16° for each model variable were forced at the surface by 11 different monthly mean wind stress climatologies.

The model coastline was interpolated from the 1/12° ETOP05 bottom topography (National Oceanic and Atmospheric Administration (NOAA), 1986) to the model grid using an “influence radius interpolation technique” (Alan J. Wallcraft, personal communication). The 200-m isobath (which lies near the shelf break) forms the model boundary, except in the Gulf of Mexico where the boundary follows the 50-m isobath from the southern tip of Florida to the western side of Campeche Bank off Yucatan, Mexico (Fig. 1b) and from there, it follows the 100-m isobath around Campeche Bank. Hurlburt and Thompson (1980, 1982) show that in a fully nonlinear model, northward penetration of the Loop Current and, consequently, eddy shedding might be prevented by not allowing the Loop Current to intrude onto the Florida shelf and Campeche Bank at depths shallower than 200 m. The 1/16° interpolated model boundary was then modified as described by McManus et al. (1997) for more accurate representation of the complicated Caribbean and Bahamas geometry (Fig. 1c and d).

The model parameters are given in Table 1. The mean thickness of the active upper layer is 250 m and the domain-averaged stratification of 1.76 kg m⁻³ was derived from the Levitus (1982) oceanic climatology, choices which affect the mean sea surface height but not the streamfunction for the mean flow in these linear simulations. For the model formulation used here, the results depend on the particular wind forcing data set applied, the eddy viscosity, the model geometry, and the model grid resolution. In one additional simulation using the same 1/16° model, the linear solution of the upper ocean portion of the North Atlantic thermohaline circulation was computed by imposing a constant 14 Sv northward mass flux through the northern and southern boundaries

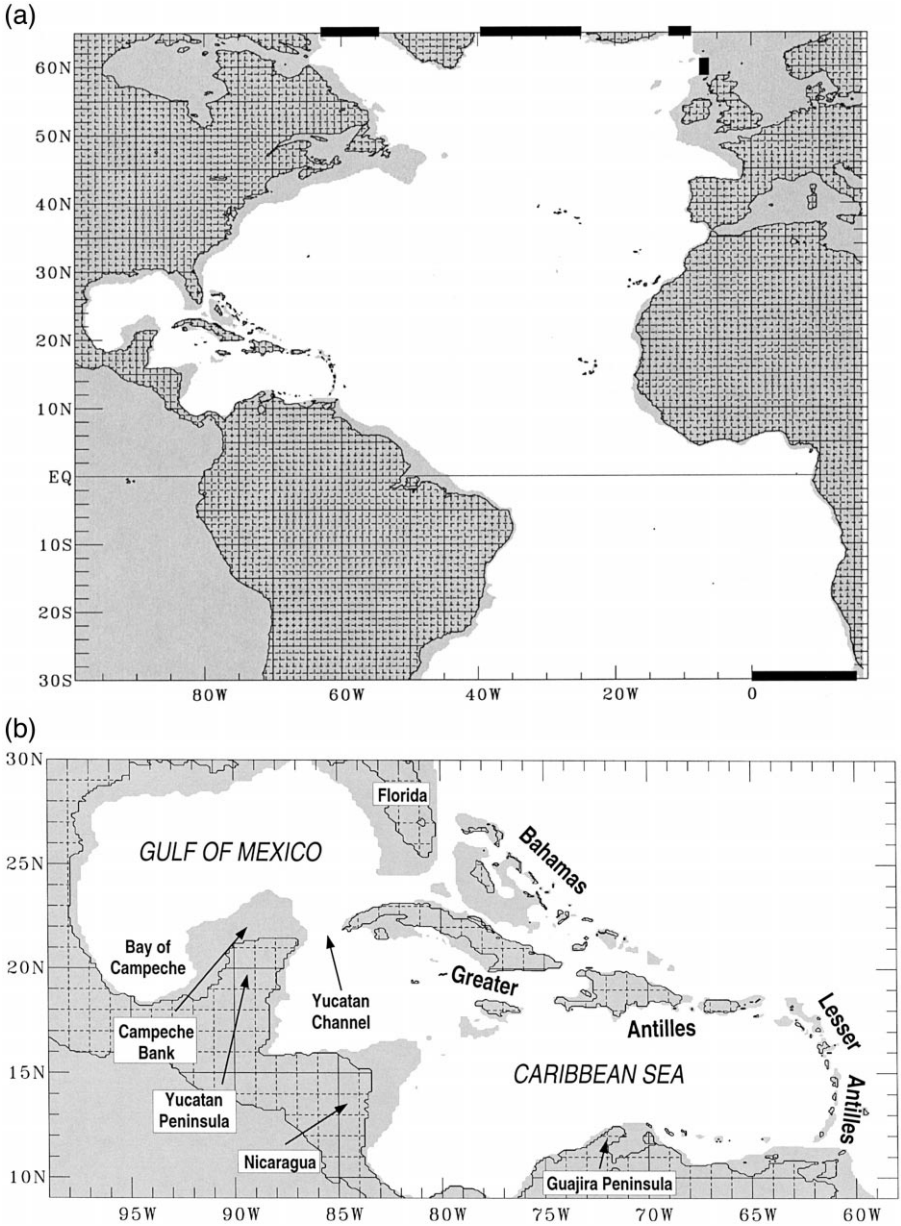


Fig. 1. (a) Full model domain. The model land/sea boundary is the 200-m isobath, except in the Gulf of Mexico. Also shown (black boxes) are the southern boundary inflow port and northern boundary outflow ports, which are open in the linear thermohaline-driven simulation (Table 2). (b) Geography of the IAS region of the NLOM of the Atlantic basin. (c) As in (b), but for the Bahamas and Greater Antilles region of the IAS. (d) as in (c), but for the Lesser Antilles region of the IAS.

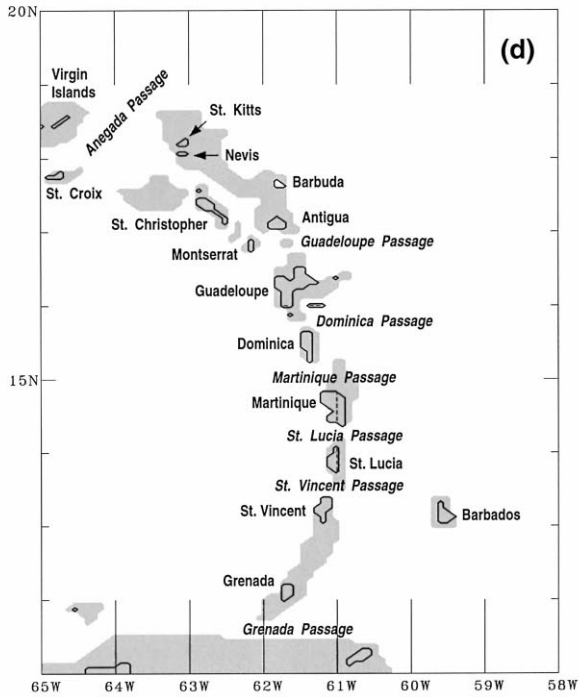
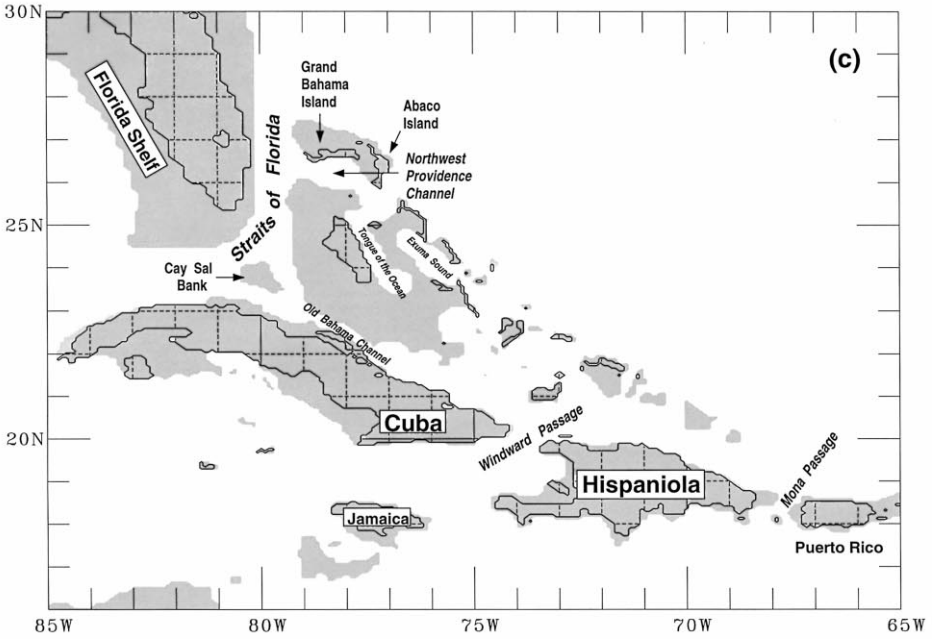


Fig. 1 (continued).

Table 1
Model parameters

Parameter	Value	Definition
A_H	$30 \text{ m}^2 \text{ s}^{-1}$	coefficient of horizontal eddy viscosity
H_k	$250/\infty \text{ m}$	k th layer thickness at rest
C_k	0	coefficient of interfacial friction
g	9.8 m s^{-2}	acceleration due to gravity
ρ_k	$25.98/27.74\sigma_T$	k th layer density, constant in space and time
$\Delta\theta, \Delta\phi$	$1/16^\circ, 45/512^\circ$ (7 km at 45°N)	latitude, longitude grid resolution

(Fig. 1a) and omitting the wind forcing. The location and amplitude of the specified transports (Table 2) were ascertained from observations (e.g., Schmitz, 1996; Schmitz and Richardson, 1991; Schmitz and McCartney, 1993; Mauritzen, 1993).

3. Wind forcing data sets

Since Sverdrup (1947) first used the relationship between wind stress curl and oceanic mass transport to investigate the ocean circulation, atmospheric data sets have steadily improved and currently range from climatologies formed by using statistical analyses of marine wind observations to those formed from global analyses produced by assimilating a wide variety of data into operational atmospheric models. In the latter, the analyses are influenced by dynamical and physical constraints (such as orography) in the atmospheric model. In addition to sparse wind data over the ocean, there are systematic errors in estimating the wind speed from ship observations, either when adjusting anemometer measurements to a constant level or using the Beaufort equivalent scale to determine wind speed. The World Meteorological Organization (WMO) (1970) and Kaufeld (1981) report that wind speeds below Beaufort 8 are systematically underestimated and those above are overestimated. Another potential source of error in these surface stress climatologies is the value used for the drag coefficient, C_D . Wind stress climatologies derived from atmospheric models are also impacted by observed wind speed errors since they assimilate observations. The operational model-based analyses suffer from omission of data not made available in near real time as well as temporal inconsistencies due to changes in the atmospheric model, data assimilation system and analysis techniques. These problems have been alleviated in the re-analyses of the

Table 2
Port transports and locations in linear simulation of upper thermohaline circulation

Port parameter	Southern boundary	Northern boundary			
Transport ($1 \text{ Sv} = 10^6 \text{ m}^3 \text{ s}^{-1}$)	14 Sv	2 Sv	3 Sv	2.7 Sv	6.3 Sv
Location	0°E to Africa	Davis Strait	Denmark Strait	Iceland-Faeroes Ridge	Shetland Channel

historical database by current versions of operational atmospheric model and data assimilation systems. Other potential problems with model-based products are grid resolution, model physics, data assimilation methods, first guess errors, and the fact that averaging of many sparse data analyses allows model dynamics to have a significant impact on the climatological mean.

For this comparison of Sverdrup solutions, 11 different wind stress data sets, summarized in Table 3, were used to force the model, eight derived from interannual time series. These include four wind stress climatologies derived entirely from observations, four generated from operational atmospheric model nowcasts, and three re-analysis products formed from current and fixed-in-time versions of operational atmospheric forecast models. The purpose in choosing each of these wind sets is discussed in Section 3.1. Since the wind stress climatologies cover different time periods and have varying durations, similarities in the Sverdrup solutions from these wind sets further support explanations of some large-scale observed circulation features based on Sverdrup dynamics. Also, the wind stress data sets, as they are used here, are often used to force numerical ocean models. The linear solutions provide, therefore, a baseline for comparison by ocean modelers to their nonlinear results obtained from any one of these same wind forcing data sets. All wind stress products were interpolated from their native grids (described below) to the $1/16^\circ$ North Atlantic NLOM grid using cubic splines.

3.1. Wind forcing data set descriptions

3.1.1. Hellerman–Rosenstein

Over the last decade or so, in addition to being used to compute Sverdrup transports for comparison with measured transport values, the HR monthly mean wind stress climatology has been commonly used to force large-scale ocean models, although others have been investigated for this purpose (e.g., Böning et al., 1991a,b; Rienecker et al., 1996) and similarly for the Mediterranean Sea (Myers et al., 1998). HR's compilation of 106 years of surface marine data from 1870 through 1976 was the first global wind stress climatology derived from surface observations rather than wind rose data or statistical information on wind speed frequencies in each direction (e.g., Hellerman, 1967, 1968). HR acknowledged the various suggested values and formulations of C_D , but claimed that it was not determined which is appropriate for the computation of large-scale wind stress. They used the same parameterizations as Bunker (1976) (BU hereafter) who first used the National Climatic Center Voluntary Observing Fleet data to generate a monthly mean wind stress climatology over the Atlantic for the period 1941–1972. BU's drag coefficient formulation is dependent on wind speed and atmospheric stability. Both smoothed (HRSM hereafter, Fig. 2a) and unsmoothed (HRUNSM hereafter, Fig. 2b) versions of the HR wind stress climatology were used to drive the $1/16^\circ$ linear model. HRSM was created by smoothing HRUNSM with one pass of a nine-point smoother on the original grid to eliminate two grid interval noise. This noise is not seen when wind stress curl is calculated using centered differences on the original $2^\circ \times 2^\circ$ grid (e.g., Fratantoni et al., 2000), but it is very apparent when HR is interpolated to the finer ocean model grid and the curl is then calculated (as was done

Table 3

Wind stress data set information summary. Each wind set was used to force a $1/16^\circ$ linear, 1.5-layer, hydrodynamic, reduced gravity version of NLOM and thus determine the North Atlantic Sverdrup flow and Munk western boundary layers

Wind data set	Reference	Type	Time period	Grid	Derivation technique
HR, smoothed	Hellerman and Rosenstein, 1983	Surface marine observation (mostly wind estimates)	1870–1976	$2^\circ \times 2^\circ$ global	Bulk aerodynamic formula using WMO Beaufort equivalent scale and parameterizations similar to BU As above
HR, unsmoothed	Hellerman and Rosenstein, 1983	Surface marine observation (mostly wind estimates)	1870–1976	$2^\circ \times 2^\circ$ global	As above
UWM-COADS	da Silva et al., 1994a,b	Surface marine observation (mostly wind estimates)	1945–1989	$1^\circ \times 1^\circ$ global (excl. Antarctica)	Bulk aerodynamic formula using revised Beaufort equivalent scale to reduce wind speed bias.
IH	Isemer and Hasse, 1987	Surface marine observation (mostly wind estimates)	1941–1972	$1^\circ \times 1^\circ$ N. Atlantic	Similar to BU, except used a revised Beaufort equivalent scale and reduced C_D
ECMWF 1000 mb	ECMWF, 1995	Operational atmospheric model nowcasts	1981–1993	$2.5^\circ \times 2.5^\circ$ global	Bulk aerodynamic formula using 12-hourly u and v , $C_D = 1.5 \times 10^{-3}$, and $\rho_{\text{air}} = 1.2 \text{ kg/m}^3$
ECMWF 10 M	ECMWF, 1995	Operational atmospheric model nowcasts	1985–1994	$2.5^\circ \times 2.5^\circ$ global	As above, except using 10 m u and v
ECMWF 1000 mb	ECMWF, 1995	Operational atmospheric model nowcasts	1983–1986	$2.5^\circ \times 2.5^\circ$ global	As ECMWF 1000 mb data set above, but for a more limited time period
ECMWF 1000 mb re-analysis	Gibson et al., 1997	Static, up-to-date atmospheric model analyses	1979–1993	$2.5^\circ \times 2.5^\circ$ global	Same as 1000 mb ECMWF data sets above, except using six-hourly re-analyzed u and v wind components
ECMWF 10 m re-analysis	Gibson et al., 1997	Static, up-to-date atmospheric model analyses	1979–1993	$2.5^\circ \times 2.5^\circ$ global	As ECMWF 10 m data set above, except using six-hourly re-analyzed u and v
FNMO surface stresses	Hogan and Rosmond, 1991	Operational atmospheric model nowcasts	7/90–6/95	$1.25^\circ \times 1.25^\circ$ global	As generated by the Navy Operational Global Atmospheric Prediction System (NOGAPS)
NCEP surface stress re-analysis	Kalnay et al., 1996	Static, up-to-date atmospheric model analyses	1979–1995	$2.5^\circ \times 2.5^\circ$ global	As generated by the NCEP Project atmospheric model–data assimilation system

with all of the wind stress curl fields shown in Fig. 2). Both the HRSM and HRUNSM were used to force the linear model to investigate effects of the noise and tradeoffs between using the noisy wind stress curl with stronger gradients for large-scale features and a smooth wind stress curl field with weaker gradients.

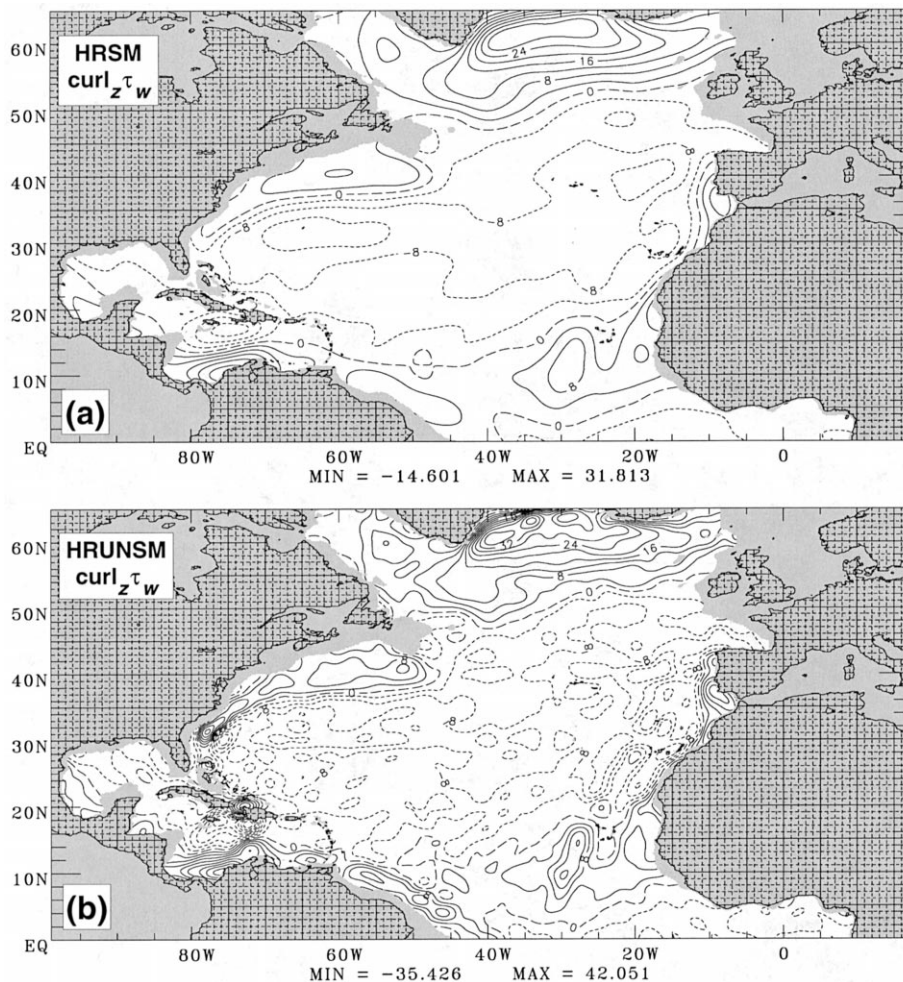


Fig. 2. Annual mean wind stress curl over the North Atlantic interpolated to the $1/16^\circ$ model grid from (a) Hellerman and Rosenstein (1983) after smoothing with one pass of a nine-point filter on the original 2° grid, (b) unsmoothed HR, (c) UWM-COADS (da Silva et al., 1994a,b), (d) Isemer-Hasse (IH, 1987), (e) European Centre for Medium-Range Weather Forecasting (ECMWF) (1995) 1981–1993 1000 mb winds, (f) ECMWF 1983–1986 1000 mb winds, (g) ECMWF 1985–1994 10 m winds, (h) ECMWF 1979–1993 1000 mb re-analysis, (i) ECMWF 1979–1993 10 m re-analysis winds, (j) FNMOG 7/90–6/95 surface wind stresses, and (k) NCEP [1996] 1979–1995 re-analysis monthly mean wind stress climatologies. The contour interval is $4 \times 10^{-8} \text{ N m}^{-3}$. Negative wind stress curl values are indicated by short dash lines and the long dash line delineates the zero curl line.

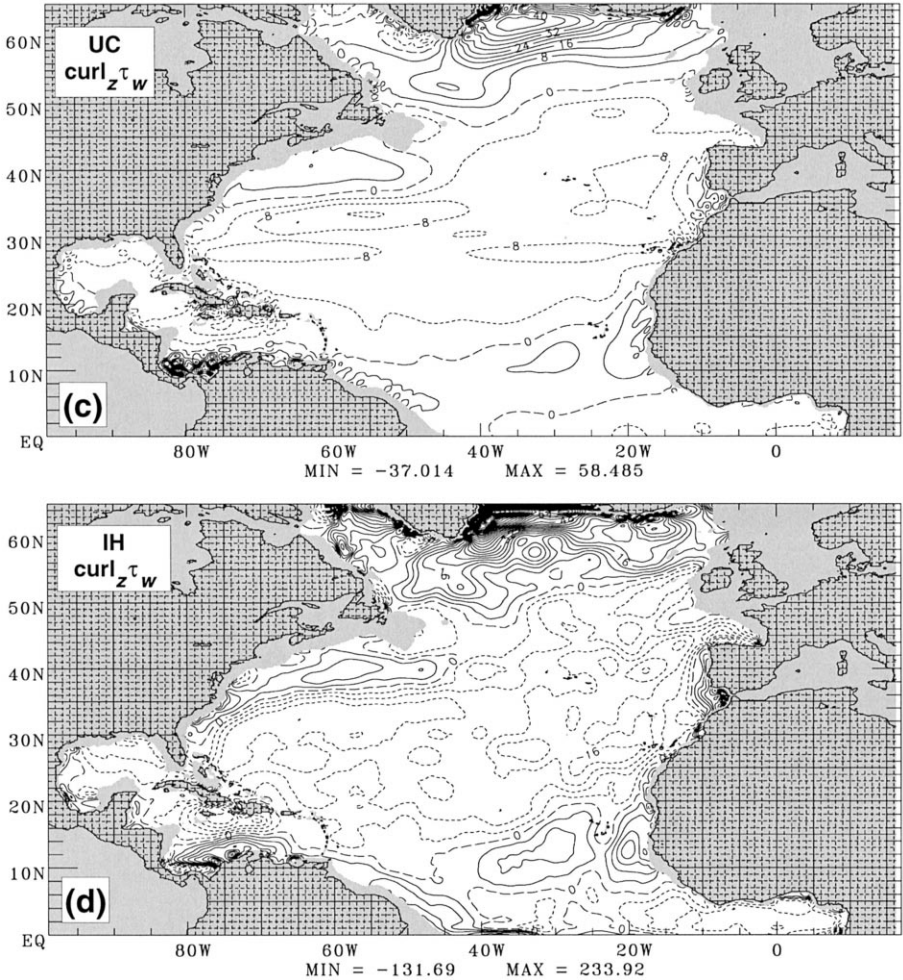


Fig. 2 (continued).

3.1.2. UWM-COADS

At the University of Wisconsin-Milwaukee (UWM), da Silva et al. (1994a,b) developed a new Beaufort equivalent scale which they utilized to improve the estimated wind speeds of individual observations in the Comprehensive Ocean-Atmosphere Data Set (COADS) described by Woodruff et al. (1987). Like HR, COADS is also widely used in studies of large-scale ocean dynamics and to force numerical ocean models. da Silva et al. (1994a,b) also improved the resolution of the standard COADS analysis, which is on a $2^\circ \times 2^\circ$ grid, by objectively analyzing the individual COADS observations from 1945 to 1989 on a $1^\circ \times 1^\circ$ global grid, excluding Antarctica. Using a stability dependent value for C_D , they computed wind stresses and formed a monthly mean wind stress climatology. See Fig. 2c for the UWM-COADS (UC, hereafter) annual mean wind

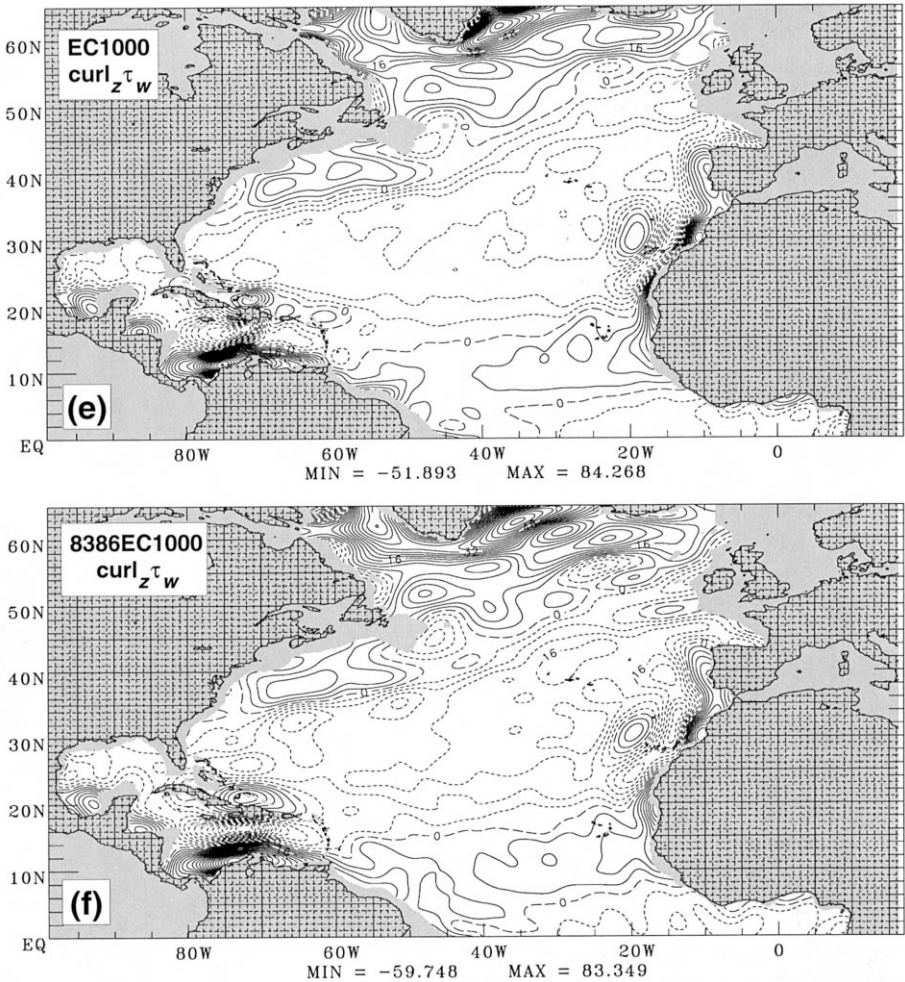


Fig. 2 (continued).

stress curl field. Grid interval noise is found in some areas bordered by complicated land areas.

3.1.3. Isemer–Hasse

Isemer and Hasse (1985) first interpolated BU’s 1941–1972 monthly mean North Atlantic data from his irregularly shaped averaging elements to a $1^\circ \times 1^\circ$ grid without making any bias corrections. Then, they used a revised set of parameterizations in the development of North Atlantic air–sea interaction data sets for this time period (Isemer and Hasse, 1987, IH hereafter). Their updated parameterizations for the climatological wind stress yielded the opposing effects of smaller drag coefficients and significantly higher wind speeds for those wind estimates below Beaufort 8. The higher wind speeds

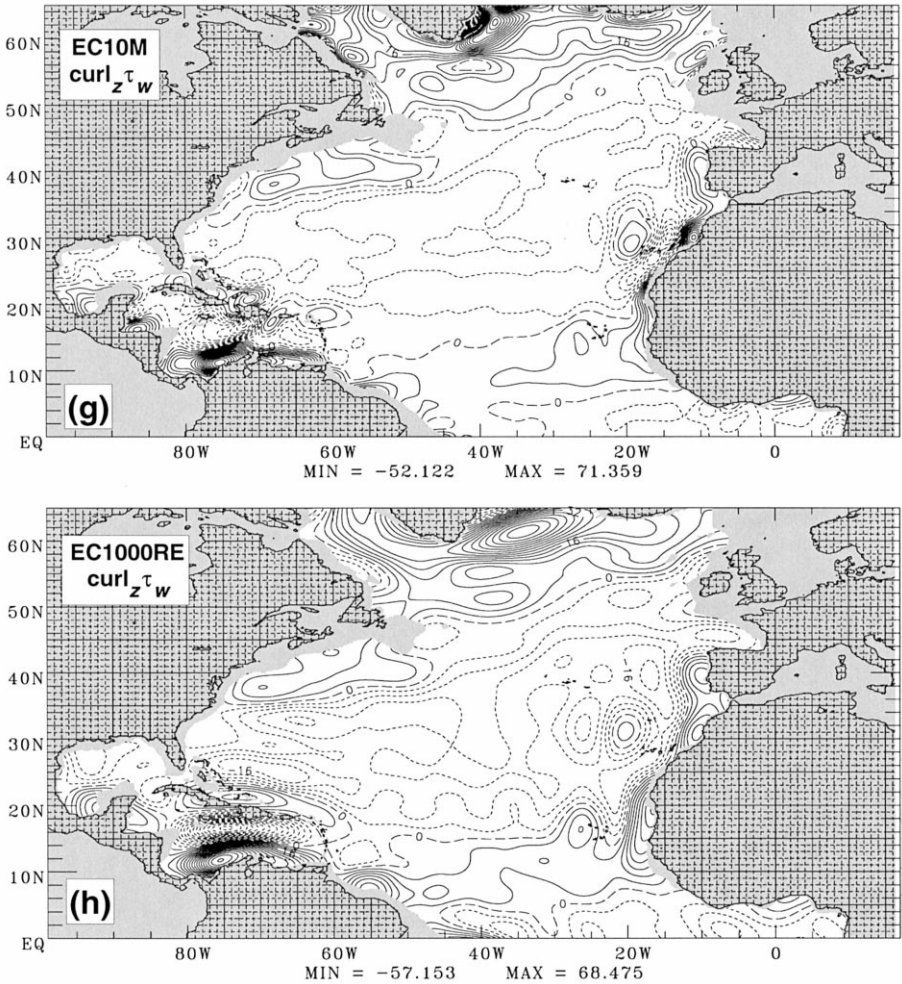


Fig. 2 (continued).

that occurred throughout the North Atlantic in each month resulted from using the improved Beaufort scale of Kaufeld (1981). Opposing the effect of higher wind speeds on the calculation of the wind stress were the reduced drag coefficients applied by IH based on their assessment that BU's values were 21% too high. One additional revision to the drag coefficients by IH resulted from their use of virtual temperature difference between air and sea, rather than the air–sea temperature difference, in order to account for the influence of humidity on the vertical density gradient. This gives a more unstable density stratification than that given by the air–sea temperature difference, thereby increasing the drag coefficient. Böning et al. (1991a), however, noted that the effect of this on the mean wind stress is “an order of magnitude smaller” than the use of a revised Beaufort equivalent scale and the 21% reduction of BU's drag coefficients. The

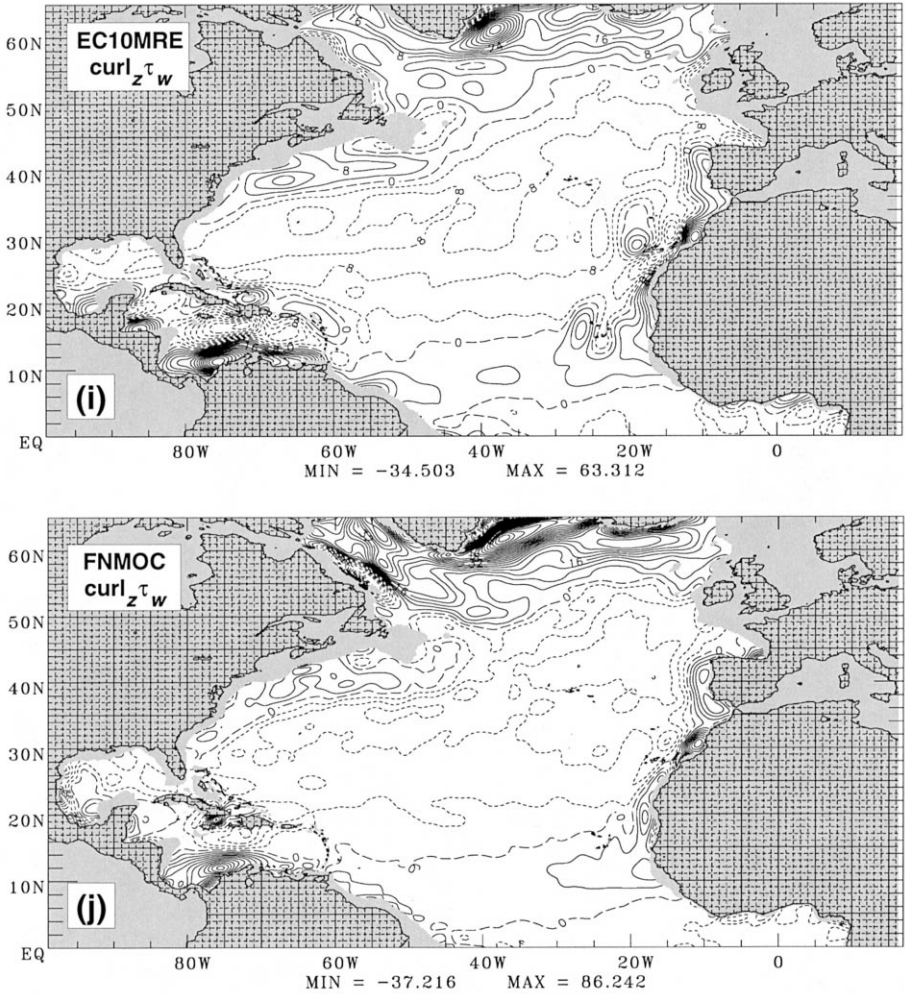


Fig. 2 (continued).

IH winds (Fig. 2d) have been used in nonlinear Atlantic Ocean models (e.g., Böning et al., 1991a,b) and we include the linear model results here for comparison.

3.1.4. ECMWF

Monthly climatologies derived from both the European Centre for Medium-Range Weather Forecasts (ECMWF) re-analysis and the archived operational winds were also used to force the linear model. These include three monthly mean wind stress climatologies formed from interannual time series of ECMWF operational atmospheric nowcast products. The first (Fig. 2e; EC1000, hereafter) was derived by inserting the $2.5^\circ \times 2.5^\circ$ 1000 mb 12-hourly winds with no directional changes into the standard bulk aerody-

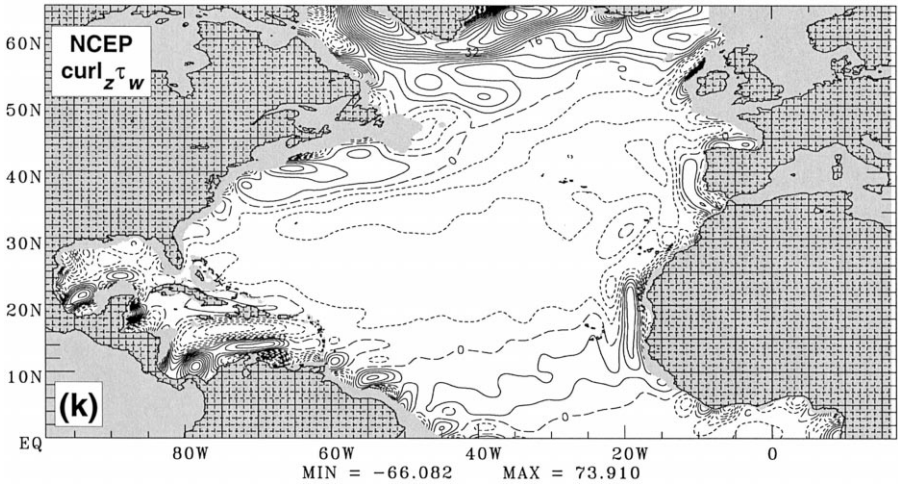


Fig. 2 (continued).

namic formula for wind stress with a constant drag coefficient of 1.5×10^{-3} and $\rho_{\text{air}} = 1.2 \text{ kg m}^{-3}$, then computing monthly averages for the period 1981 through 1993. An advantage to using this data set is that it has a relatively long time series compared to other archived operational atmospheric products. A disadvantage is that since this is an operational product, it is inconsistent through time due to changes in the atmospheric model and data assimilation system. For example, in September 1991, the atmospheric model resolution was increased to spectral T213 (0.85° along the equator) and changes were made over time in the model physics, including improvements to the surface and boundary layer processes (ECMWF, 1994, 1995). Another monthly mean wind stress climatology using the 1000 mb winds was formed in the same manner, but for the period covering 1983–1986 only (Fig. 2f; 83–86EC1000, hereafter). The annual mean over these 4 years has a larger area of positive wind stress curl on the northern side of the Gulf Stream than the EC1000 and other wind stress climatologies. Chao et al. (1996) reported that the cyclonic wind stress curl pattern for this 4-year period over the northwest Atlantic produced realistic separation of the Gulf Stream in a $1/6^\circ$ North Atlantic version of the Parallel Ocean Program (POP) (Dukowicz and Smith, 1994). One additional ECMWF nowcast-based wind stress climatology, used to force the linear model, was generated using the 10-m winds for the period 1985, when they first became available, through 1994 (Fig. 2g; EC10M, hereafter). The same methodology, C_D , and ρ_{air} were used as for the 1000-mb winds.

A newly available time series of atmospheric analyses is based on the re-analysis of historical observational data by a fixed 1994 version of the ECMWF data assimilation and operational atmospheric forecast model (Gibson et al., 1997) and it covers the time period from January 1979 through December 1993. An advantage of this data set is the length of the time series without any changes to the system, in addition to the inclusion of observations that were not available in the original nowcasts due to reporting delays. The re-analysis resolution was spectral T106 (1.7° along the equator) to conserve

resources. The results were then transformed to a $2.5^\circ \times 2.5^\circ$ grid after truncation to T47 (3.8° along the equator). Two monthly mean wind stress climatologies were generated from this data set, one using the 1000-mb winds (Fig. 2h; EC1000RE, hereafter) and one using the 10-m winds (Fig. 2i; EC10MRE, hereafter) in the same manner as in the climatologies based on the operational ECMWF nowcasts described above, except that the six-hourly analyses were used instead of the 12-hourly analyses available for the archived operational product.

3.1.5. *Fleet Numerical Meteorology and Oceanography Center (FNMOC) surface stresses*

A monthly mean climatology of surface stresses for the period from July 1990 through June 1995 was created from the FNMOC 12-hourly Navy Operational Global Atmospheric Prediction System (NOGAPS) (Hogan and Rosmond, 1991) surface stresses. This wind set is included in the comparison below because operational ocean models at FNMOC use real time wind products from NOGAPS. The grid resolution of these analyses is $1.25^\circ \times 1.25^\circ$. Prior to this time period, large effects of operational changes to NOGAPS were noted on the amplitude of the surface stresses as well as problems with the generation of the NOGAPS surface products (John C. Kindle, personal communication) and, therefore, they were not included in this wind stress climatology (Fig. 2j; FNMOC, hereafter).

3.1.6. *National Centers for Environmental Prediction (NCEP) surface stresses*

An additional global re-analysis product, that is also used to drive numerical ocean models, was used in this study. It is comparable to the ECMWF re-analysis, but created from the analysis of historical data by the NCEP. As with the ECMWF re-analysis, this product is not affected by changes in the atmospheric operational model or data assimilation technique. It is further improved from the NCEP operational nowcast product by including more atmospheric observations (Kalnay et al., 1996). For the present study, a monthly mean climatology was created using NCEP's 1979–1995 re-analyzed six-hourly surface wind stresses. These were transformed from the spectral T62 (2.9° along the equator) resolution, used for the analysis, to a $2.5^\circ \times 2.5^\circ$ grid. In the NCEP re-analysis (Fig. 2k), the surface wind stress was computed by NCEP using a drag coefficient that is a function of the bulk Richardson number.

3.2. *Wind forcing data set comparisons*

Fig. 2 reveals that the same basic annual mean wind stress curl features are present in each of the wind stress climatologies described above. Among these features is a basin-wide area of negative curl over the mid-latitudes of the North Atlantic associated with the subtropical high-pressure cell. This feature is aligned along 30°N and bounded by westerly winds to the north and easterly trade winds to the south. North of the western portion of this large area of anti-cyclonic wind stress curl (off the northeast US and southeast Canadian coasts) is an area of positive (cyclonic) wind stress curl. There are also regions of positive wind stress curl over the subpolar gyre (SPG) region associated with the Icelandic low and in the tropics centered near $5\text{--}10^\circ\text{N}$. Another

prominent feature in all of the wind sets is the pair of anti-cyclonic and cyclonic wind stress curl maxima located over the central Caribbean associated with a maximum in the easterlies. Along with basic similarities, many variations in pattern and amplitude are evident. The discussion below shows how these variations have substantial impact on the Sverdrup flow response and the associated western boundary currents.

4. Sverdrup flow results

The observed basic large-scale features of the North Atlantic surface circulation are the three gyres whose boundaries are outlined in Fig. 3. The large anti-cyclonic subtropical gyre (STG) with its axis along 30°N is bounded on the west by the Gulf Stream, the North Equatorial Current (NEC) to the south at ~15°N and the North Atlantic Current (NAC) to the north at ~50°N. The main part of this gyre extends across the North Atlantic and exhibits an observed C-shape, which is not shown in Fig. 3 (Leetmaa et al., 1977; Stommel et al., 1978; Schmitz et al., 1992), while the southwestern portion of this major gyre system flows through the Caribbean Sea and Gulf of Mexico and exits the IAS through the Florida Straits. South of the STG is the cyclonic circulation which forms the northern tropical gyre (NTG) with the NEC on the north and North Equatorial Counter Current (NECC) on the south at ~5°N. The cyclonic SPG lies between the STG and the polar regions and is bounded by the NAC on the south, the Irminger Current, which flows northward along the eastern limb, the

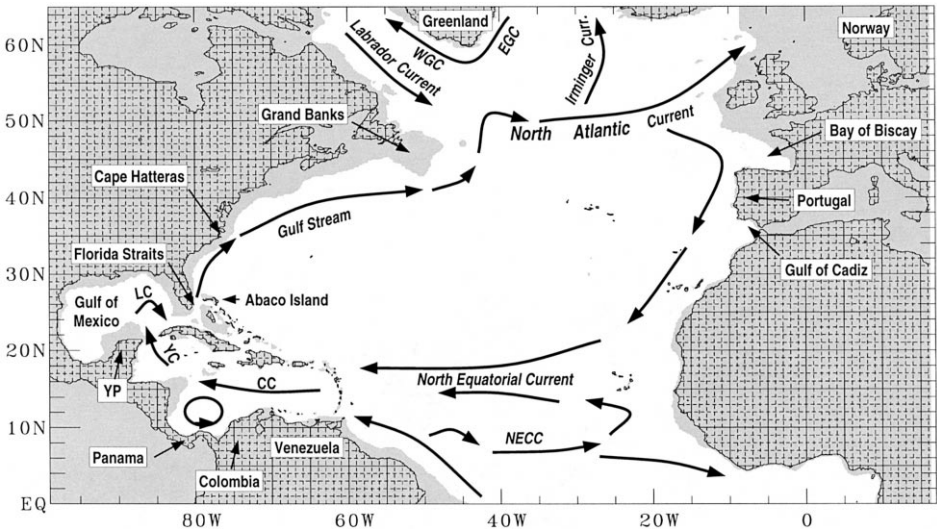


Fig. 3. Schematic of the North Atlantic surface circulation showing the boundaries of the major gyres and some of the large-scale currents. YP = Yucatan Peninsula; NECC = North Equatorial Counter Current; YC = Yucatan Current; LC = Loop Current; EGC = East Greenland Current; WBC = West Greenland Current.

East and West Greenland Currents to the north (EGC and WGC, respectively), and the Labrador Current, which flows southward in the western portion of the SPG. In the IAS, the major features are the Caribbean Current, the cyclonic circulation in the southwest Caribbean Sea off Panama and Colombia, and the Yucatan Current, which flows northward along the Yucatan peninsula from the Caribbean Sea to feed into the Loop Current. The Loop Current penetrates northward into the Gulf of Mexico and sheds large anti-cyclonic eddies with nearly annual frequency (Vukovich, 1995). There is also an anti-cyclonic wind-driven circulation in the northern Gulf of Mexico and a cyclonic gyre in the Bay of Campeche west of the Yucatan peninsula.

These major circulation features, including the westward intensification of the flow (Stommel, 1948), are simulated by the linear model when it is forced by each of the previously described wind stress forcing fields. However, many aspects vary substantially with the different wind forcing fields and they differ from what is known about them based on observations. A notable example is the C-shape of the STG produced by the different wind sets. Also, in the wind-driven only (i.e., there is no thermohaline component to the flow) Sverdrup solution, the cyclonic NTG, as discussed later in Section 4.1.3, lies partly in the southern Caribbean Sea with inflow through all but one of the southern passages of the Lesser Antilles. The returning eastward flow in the southern branch of the gyre leaves the Caribbean through the Grenada Passage (Fig. 1d).

4.1. Sverdrup flow within the major gyre systems

4.1.1. The subtropical gyre

The results in Fig. 4 and Table 4 show that the maximum Sverdrup transport in the STG varies from greater than 40 Sv when the model is driven by the HRUNSM, IH, and EC1000RE monthly mean wind stress climatologies to 23 Sv when it is forced by the NCEP monthly mean wind stress climatology. The simulations forced by the UC winds, EC10M operational nowcast, EC10MRE re-analysis winds, and the FNMOC surface stresses have a STG transport of 26–28 Sv. The results from HRSM and the EC1000 wind stress climatologies are greater than 30 Sv. The location of the western edge of the boundary between the STG and SPG also varies depending on the wind forcing from 48°N in the 83–86EC1000 simulation to 50°N in the FNMOC simulation (Table 4).

4.1.1.1. The Gulf Stream. In a significant departure from the single observed mean pathway from Cape Hatteras to the Grand Banks shown in Fig. 3, the Gulf Stream in each of the linear simulations has two mean paths (Fig. 4), except in the HRUNSM simulation (Fig. 4b), which has three. One separates from the coast at Cape Hatteras and penetrates due east in an unrealistic manner and the other path overshoots the observed separation point at Cape Hatteras and continues to flow northward along the continental boundary (Fig. 4) then eastward adjacent to the regional northern boundary, which extends eastward as far as the Grand Banks of Newfoundland.

Why does the Gulf Stream split into two branches in the Sverdrup solution? The overshooting/boundary-hugging current is compensation for that part of the southward Sverdrup flow east of about 45°W, 40°N that is not balanced by the northward flow between the western boundary and the anti-cyclone centered at 41°N, 42°W (Mann,

1967). There is insufficient northward flow on the north side of the southern Gulf Stream branch to balance the southward Sverdrup transport east of 45°W when integrated from the eastern boundary along this latitude to the east side of the western boundary current. Consequently, the associated western boundary current must be to the north. Clearly, a major addition to the linear dynamics of the Sverdrup relation is required to explain the observed nonlinear Gulf Stream pathway between Cape Hatteras

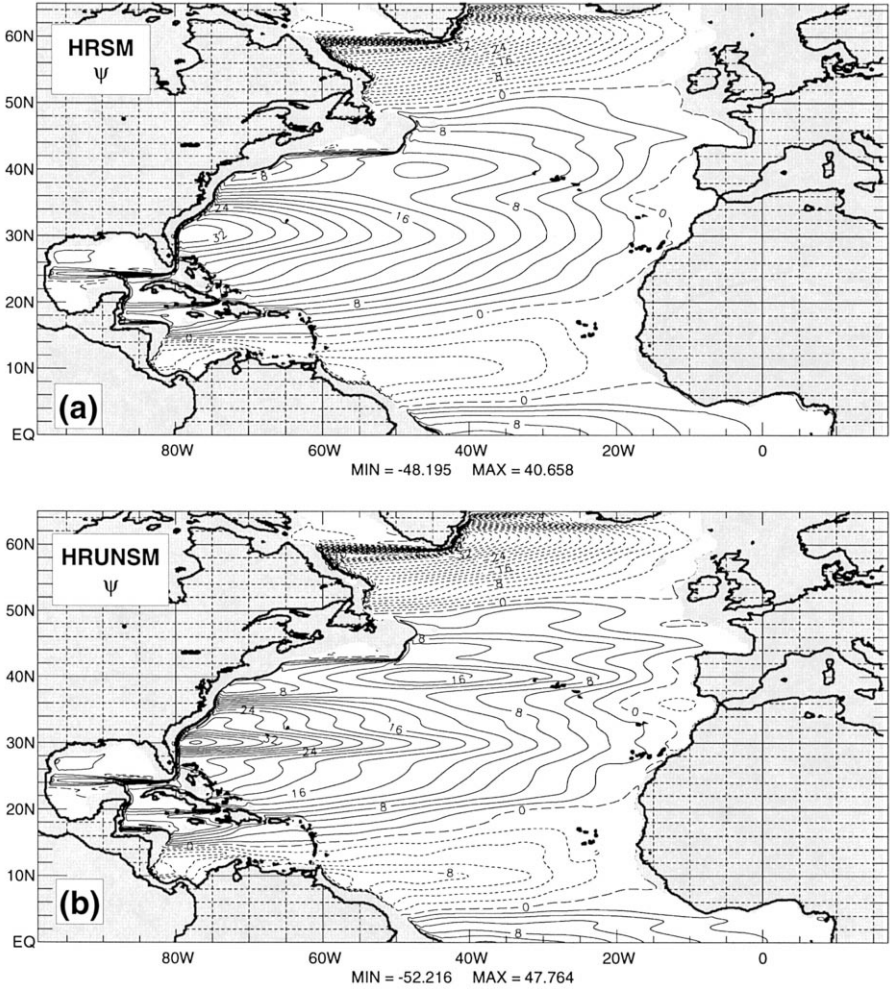


Fig. 4. Annual mean upper layer streamfunction over the North Atlantic from the 1/16°, 1.5-layer, linear NRL model of the Atlantic Ocean north of 30°S forced by the (a) smoothed HR, (b) unsmoothed HR, (c) UWM-COADS, (d) IH, (e) ECMWF 1981–1993 1000 mb, (f) ECMWF 1983–1986 1000 mb, (g) ECMWF 1985–1994 10 m, (h) ECMWF 1979–1993 1000 mb re-analysis, (i) ECMWF 1979–1993 10 m re-analysis, (j) FNMOC 7/90–6/95 surface, and (k) NCEP 1979–1995 re-analysis monthly mean wind stress climatologies. The contour interval is 2 Sv with short dashes for cyclonic flow, long dashes for zero, and solid lines for anti-cyclonic flow.

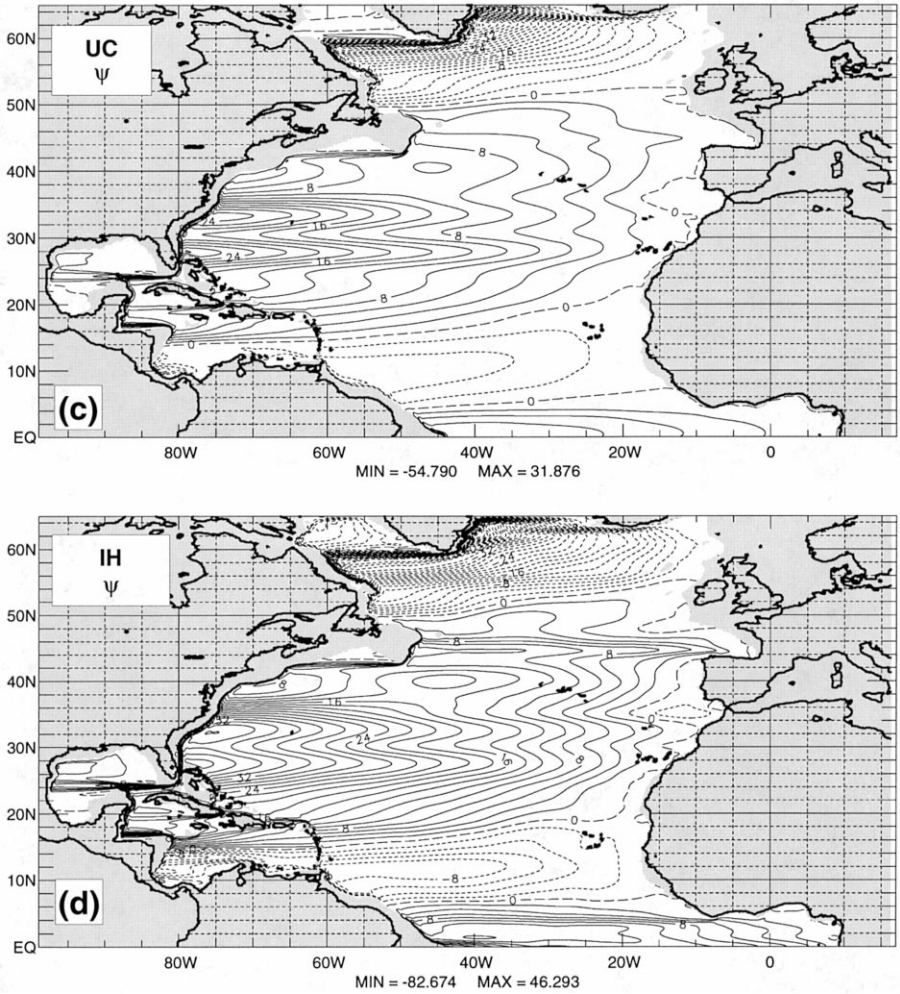


Fig. 4 (continued).

and the Grand Banks, which completely separates from the coast at Cape Hatteras. A similar two-pathway depiction of the Gulf Stream is commonly seen in the mean flow of nonlinear, eddy-resolving basin-scale models of the North Atlantic Ocean (Bryan et al., 1995; Dengg et al., 1996; DYNAMO Group, 1997; Ezer and Mellor, 2000; Hurlburt and Hogan, 2000 (their $1/8^\circ$ results), this issue). The similarity to the Sverdrup solution suggests that an $O(1)$ change in the dynamics of these models is needed to realistically simulate the Gulf Stream pathway.

The various wind sets yield Sverdrup transports (Table 5) in the southern branch of the linear Gulf Stream solution which vary from 16 Sv in the EC10MRE and FNMOC simulations to twice as much in the IH case. Conversely, while the FNMOC simulation has the smallest southern branch transport, it has the largest transport in the northern

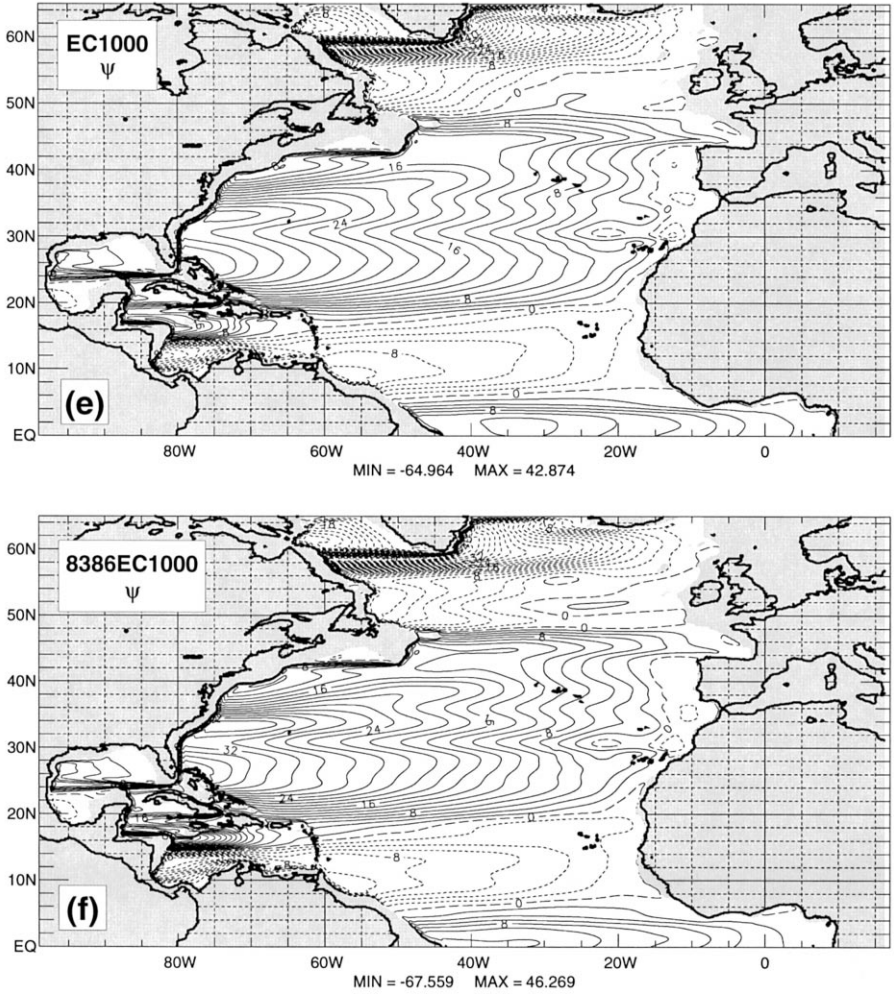


Fig. 4 (continued).

branch, 11 Sv, as measured just north of Cape Hatteras, yielding the largest percentage of overshoot. The UC and NCEP forcing produce the weakest northward western boundary transport and smallest percentage of overshoot north of Cape Hatteras.

4.1.1.2. The C-shape. In both the HRSM and HRUNSM simulations (Fig. 4a and b, respectively), there is a single transport maximum at the western boundary of the STG which is located at 30°N. Neither exhibits the C-shaped Sverdrup transport contours shown by Schmitz et al. (1992) to be similar in pattern and scale to the observed dynamic height contours shown by Leetmaa et al. (1977) and Stommel et al. (1978). However, it can be achieved in a model forced by HRSM (Fig. 2a) with the addition of

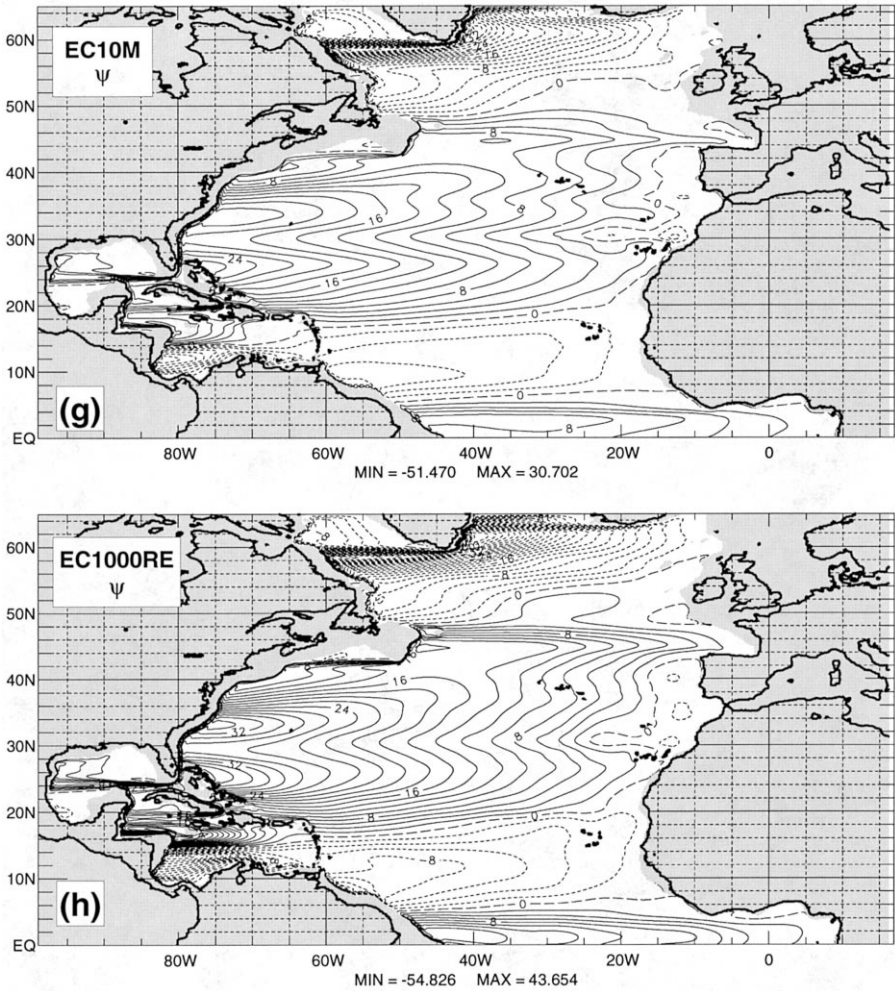


Fig. 4 (continued).

nonlinearity (Hurlburt and Hogan, 2000, this issue). All of the other wind forcing sets produce a cyclonic circulation in the Sverdrup transport contours aligned along 30°N that contributes to the observed C-shape (Fig. 4c–k). The axis of this cyclonic feature penetrates all the way across the basin to the western boundary in the UC (Fig. 4c), IH (Fig. 4d), ECMWF (Fig. 4e–i), and NCEP (Fig. 4k) simulations resulting in a double transport maximum at the western boundary, although its latitudinal extent in the NCEP simulation is broader and it is less distinct than in the others. In the FNMOC simulation (Fig. 4j), the wedge along 30°N does not extend all the way across the basin to the western boundary. The result is a single western boundary transport maximum of 30 Sv at ~33°N and the lack of a C-shaped STG in this simulation.

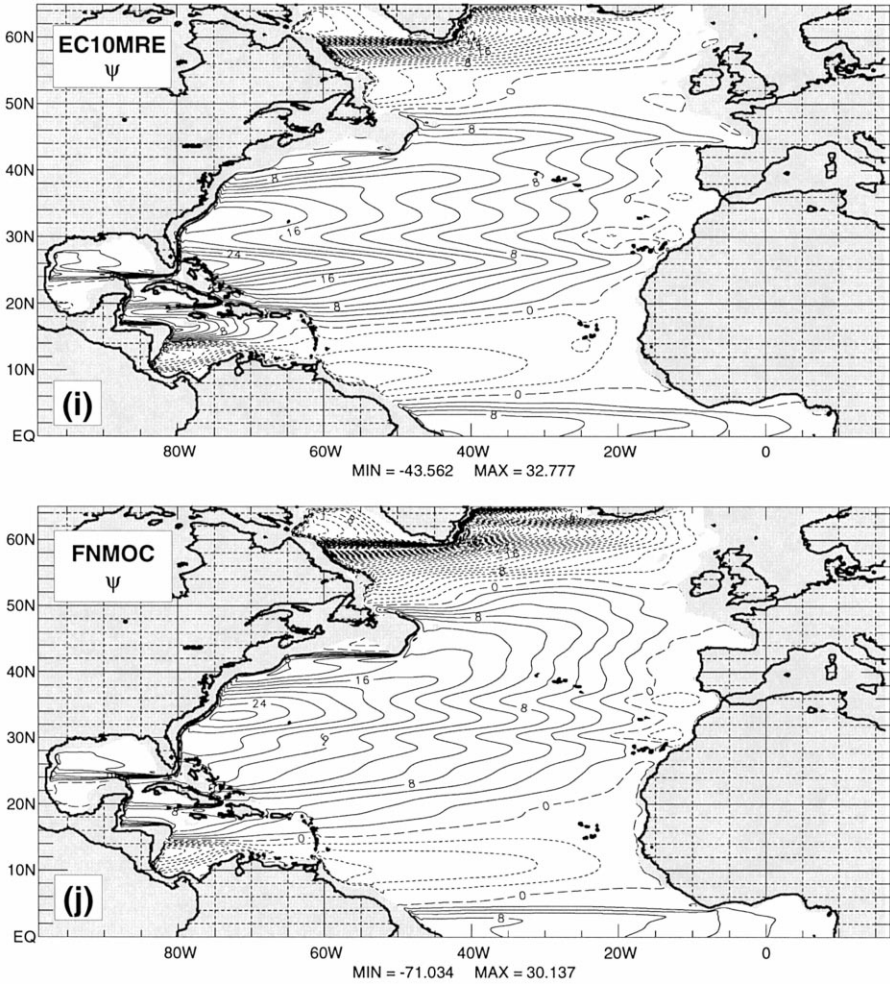


Fig. 4 (continued).

Three mechanisms are identified which can contribute to Sverdrup flow with a C-shape in the STG. The first involves a pair of positive (cyclonic) wind stress curl maxima in the eastern STG along approximately 30°N separated by a narrow area of negative wind stress curl. This pattern is evident in all the wind stress climatologies formed from global atmospheric model analyses (ECMWF, FNMOC, and NCEP; Fig. 2e–k), although it is very weak in the NCEP product (Fig. 2k). In the FNMOC surface stress climatology (Fig. 2j), the westernmost of these two wind stress curl extremes is weakly negative, not positive. In each of the ECMWF wind sets (Fig. 2e–i), there is also an anti-cyclonic wind stress curl maximum along this latitude located at about 25°W adjacent to the westernmost positive wind stress curl maximum in this region. Thus, the

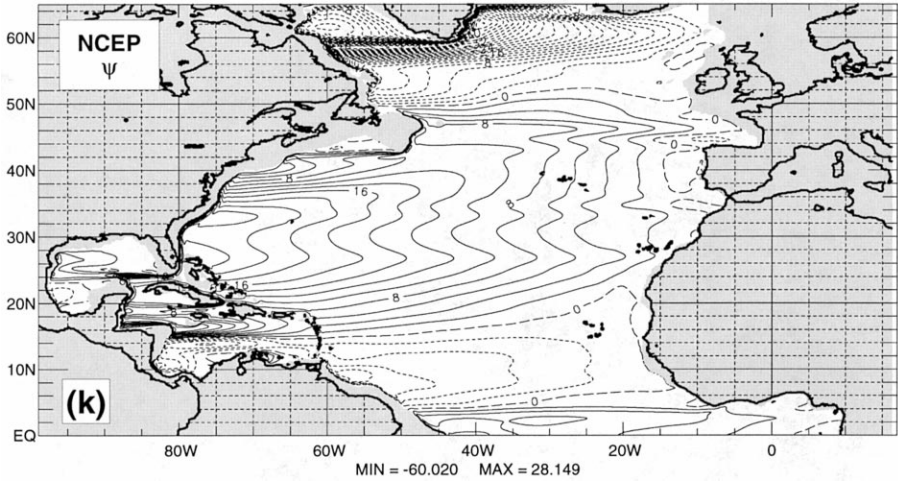


Fig. 4 (continued).

sign of the wind stress curl along 30°N in these wind sets (Fig. 2e–i) changes three times between Africa and $21\text{--}22^{\circ}\text{W}$. The larger amount of positive wind stress curl along 30°N due to the two maxima results in a greater amount of northward flow in the eastern part of the STG along this latitude than is found to the immediate north and south where only the positive wind stress curl maximum adjacent to the eastern boundary is found. The resulting Sverdrup transport streamfunction pattern in this region of the North Atlantic has an area of northward mass transport along the eastern boundary. West of this are two lobes of southward mass transport separated at 30°N by a wedge of weaker southward transport. In the ECMWF (Fig. 2e–i) and NCEP (Fig. 2k) wind stress climatologies, this is the largest contributing factor to the development of the STG C-shape (Table 5). In the FNMOC surface stress climatology (Fig. 2j), this effect is limited to the eastern STG between approximately 28°N and 32°N . The wind stress climatologies developed by statistical analysis of marine wind observations (HRSM, HRUNSM, UC, and IH; Fig. 2a–d), which depend entirely on data that may be averaged over a fairly large area, do not exhibit this pattern of two positive wind stress curl features in the eastern STG at 30°N . The wind fields from data-assimilative atmospheric models (ECMWF, FNMOC, and NCEP; Fig. 2e–k), on the other hand, include model-induced effects of coastal orography, which can have a substantial impact on the wind field. The IH wind stress climatology (Fig. 2d) has a very localized and isolated positive wind stress curl feature adjacent to the African coast at 30°N , which partly explains the C-shape in this solution (Fig. 4d).

The second mechanism contributing to the STG C-shape amplitude is the dual zonal bands of anti-cyclonic wind stress curl south of the Gulf Stream separated by a band of weaker anti-cyclonic wind stress curl. This curl pattern is not present in the HRSM, HRUNSM and NCEP wind sets (Fig. 2a,b,k, respectively), but it is found in all the others. In the UC wind stress climatology (Fig. 2c), it is particularly distinct and extends

Table 4

Large-scale gyre boundaries and transports of the North Atlantic Sverdrup/Munk solutions from 11 different wind sets. These were calculated numerically using a linear, $1/16^\circ$, 1.5-layer, hydrodynamic, reduced gravity version of NLOM covering the Atlantic Ocean north of 30°S , including the Caribbean Sea and Gulf of Mexico

Wind forcing data set	SPG transport	SPG/STG boundary ^a	STG transport ^b	STG/NTG boundary ^c	NTG transport
HRSM	37	49°N	33 at 30°N	15°N	9
HRUNSM	41	49.5°N	41 at 30°N	15°N	11
UWM-COADS	42	49.8°N	25 at 33°N 28 at 28°N	14.5°N	6
IH	57	49.9°N	39 at 32°N 41 at 28°N	15°N	8
81–93 EC1000	43	48.5°N	33 at 33°N 36 at 26°N	16°N	12
83–86 EC1000	35	48°N	35 at 33°N 39 at 26°N	16°N	14
85–94 EC10M	32	48.8°N	23 at 34°N 26 at 26°N	17°N	8
79–93 EC1000RE	45	48.5°N	35 at 33°N 40 at 26°N	16.2°N	17
79–93 EC10MRE	34	49°N	21 at 33°N 28 at 26°N	16.2°N	10
7/90–6/95 FNMOC SFC STR	61	50°N	27 at 33.5°N	15°N	8
79–95 NCEP SFC STR	44	49.5°N	23 at 33°N 23 at 27°N	14.8°N	11

^aAt the western boundary.

^bIn the case of double maxima at the western boundary of the STG, both values and their locations are given.

^cAt its intersection with the Lesser Antilles (Fig. 1b).

across the entire basin, producing 100% of the transport difference (Table 5) between the wedge and the lobes of the C-shape. In this linear simulation, the C-shape is characterized by two narrow bands of relatively strong southward flow across 28°N and 34°N separated by a narrow band of weaker southward flow across 30°N (Fig. 4c).

A third contributing factor to the C-shape can be found in the western portion of the Atlantic in each of the ECMWF wind stress climatologies. In the linear simulations forced by these wind sets, the southern part of the C-shape is further enhanced with increased southward flow by a localized anti-cyclonic wind stress curl maximum east of the Bahamas at about $70\text{--}73^\circ\text{W}$, 25°N . In four of the five linear simulations forced by ECMWF wind sets, 1–2 Sv of the C-shape amplitude results from the linear ocean response to this anti-cyclonic wind stress curl maximum (Fig. 4e–g,i, Table 5). In the EC1000RE simulation (Fig. 4h), the greater longitudinal extent of this maximum provides nearly a 5-Sv contribution to the C-shape amplitude.

4.1.1.3. The Azores Current. The Azores Current originates south of the Grand Banks of Newfoundland near the Newfoundland Rise and is an extension of the Gulf Stream (Klein and Siedler, 1989). An Azores Current is found in all but one of the linear

Table 5

Sverdrup transports for the large-scale features of the North Atlantic STG from 11 different wind stress data sets. These were calculated numerically by forcing a linear, $1/16^\circ$, 1.5-layer, hydrodynamic, reduced gravity version of NLOM covering the Atlantic Ocean north of 30°S

Wind forcing data set	STG transport ^a	Gulf Stream transport			C-shape			Azores Current transport at 33°W (eastward)
		S. Branch (eastward)	N. Branch		Transport due to eastern STG cyclonic w.s.c. pattern	Transport due to dual w.s.c. bands	Transport due to local neg. w.s.c. east of Bahamas	
			N. of CH ^b (northward)	S. of GB ^c (eastward)				
HRSM	33 at 30°N	26	7	13	–	–	–	2.00
HRUNSM	41 at 30°N	24 + 12 ^d	5	11	–	–	–	2.75
UC	25 at 33°N	22	3	9	–	7.0 (N) ^e	–	1.75
	28 at 28°N					10.0 (S) ^f		
IH	39 at 32°N	32	7	15	2.0 (N)	2.2 (N)	–	4.25
	41 at 28°N				0.6 (S)	4.0 (S)		
EC1000	33 at 33°N	24	9	15	4.4 (N)	0.4 (N)	1.8 (S)	1.00
	36 at 26°N				6.2 (S)	1.9 (S)		
8386EC1000	35 at 33°N	26	9	15	6.2 (N)	0.1 (N)	2.0 (S)	1.75
	39 at 26°N				5.4 (S)	0.7 (S)		
EC10M	23 at 34°N	18	5	9	4.25 (N)	0.75 (N)	1.6 (S)	0.75
	26 at 26°N				4.9 (S)	1.3 (S)		
EC1000RE	35 at 33°N	26	9	15	6.75 (N)	0.25 (N)	4.85 (S)	–
	40 at 26°N				5.2 (S)	2.95 (S)		
EC10MRE	21 at 33°N	16	5	9	3.2 (N)	0.30 (N)	0.90 (S)	1.20
	28 at 26°N				5.5 (S)	3.30 (S)		
FNMOC	27 at 33.5°N	16	11	15	3.3 (N)	6.75 (N)	–	2.80
					2.6 (S)	–		
NCEP	23 at 33°N	20	3	11	1.0 (N)	–	–	0.70
	23 at 27°N				2.0 (S)			

^aIn the case of double maxima at the western boundary of the STG, both values and their locations are given.

^bGulf Stream northern branch (overshoot) transport as measured north of Cape Hatteras.

^cGulf Stream northern branch transport as measured just south of the Grand Banks.

^dTransport in the third and southernmost branch of the Gulf Stream in the HRUNSM simulation.

^eN — northern lobe of C; westward transport.

^fS — southern lobe of C; eastward transport.

simulations (EC1000RE, Fig. 4h). It appears as the southern side of a westward wedge in the ψ contours along 35–36°N from 15°W to 50°W and is an eastward extension of the southern branch of the linear Gulf Stream solutions. In the simulations forced by the wind stresses derived from the atmospheric model products (except EC1000RE), this eastward extension occurs as a southern branch of the southern branch of the linear Gulf Stream (Fig. 4e–k, except 4h). The existence of an Azores Current can only be partially explained by Sverdrup dynamics since the observed Azores Current transport is about 11 Sv (Stramma, 1984) and in the linear wind-driven simulations it is only 1–2 Sv (Table 5). The associated wedge in the ψ contours is set up by relatively strong northward Sverdrup transport in the vicinity of the Gulf of Cadiz (Fig. 3) and/or a relative weakness in the southward Sverdrup transport just to the west, compared to regions immediately to the north and south. Once set up in the eastern Atlantic, this wedge would persist to the western boundary current in the presence of meridionally uniform wind stress curl to the west. In the linear simulations, it persists until the simulated Azores Current merges with the strong north–south streamfunction gradient associated with the southern branch of the linear Gulf Stream solution.

The formation of an Azores Current in the Sverdrup solution and the associated wedge in the ψ contours is illustrated by a comparison of the regional wind stress curl and the resulting Sverdrup transport for the EC1000 simulation (Fig. 5). Fig. 5b shows relatively strong northward Sverdrup transport in the Gulf of Cadiz. Integrating from east to west, southward compensation for this northward flow (at the zero streamfunction contour) occurs farthest to the west at 36°N, 16°W, resulting in the formation of the westward wedge in the basically southward Sverdrup flow of the STG. To the west of the positive wind stress curl that is adjacent to the eastern boundary, the Azores Current is relatively strong near 15°W where it is augmented by a weakness in the negative wind stress curl just north of 35°N, compared to the wind stress curl to the south and north. Between \sim 15°W and 23°W, it weakens and nearly disappears near 22°W because of the positive wind stress curl to the south. Then, it gradually strengthens again between 23°W and \sim 38°W due to the band of weaker negative wind stress curl north of 35°N compared to the areas to the north and south.

Fig. 6 shows a contrasting example for the EC1000RE simulation where no ψ wedge along 35–36°N and no Azores Current are formed. In this case, there is a weak maximum in the northward Sverdrup transport near the Gulf of Cadiz, which is counteracted by an eastward bulge in negative wind stress curl along 35–36°N at 12–15°W, immediately to the west of the positive wind stress curl. The longitude band between \sim 30°W and 40°W is the only region of relatively weak wind stress curl along 35–36°N compared to regions to the north and south, but it is insufficient to form even a weak version of the Azores Current in the linear model. In each of the 10 Sverdrup solutions which do have a linear version of the Azores Current, except in the HRSM and HRUNSM solutions, the eastern portion of the current bends southward, then westward along 31–32°N, as observed by Tychensky et al. (1996). In the linear model results, this zonal return to the west is due to the first mechanism of STG C-shape development described in the previous section, i.e., the positive wind stress curl features in this region. These wind stress curl features are absent in the HRSM and insignificant in the HRUNSM wind stress climatologies.

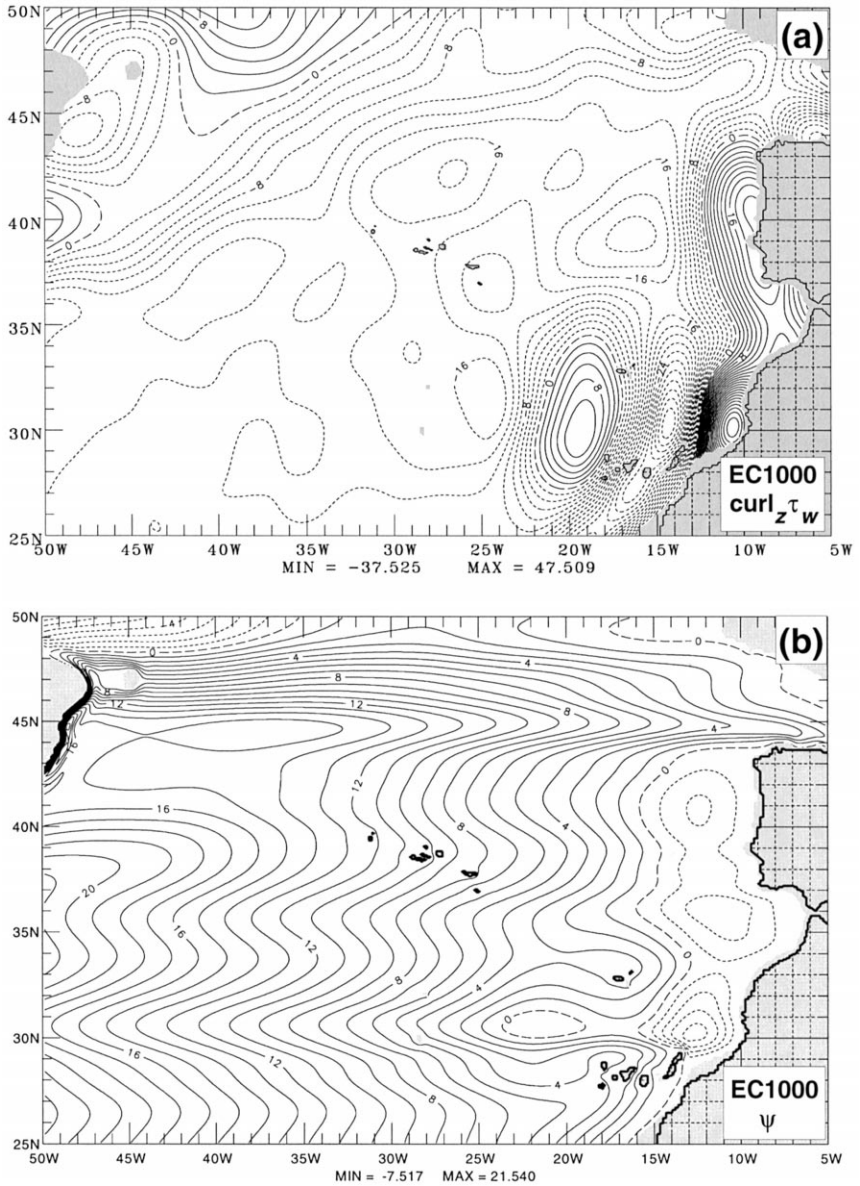


Fig. 5. Eastern STG region of the North Atlantic: (a) Annual mean wind stress curl from the ECMWF 1000 mb 1981–1993 monthly mean wind stress climatology with a $2 \times 10^{-8} \text{ N m}^{-3}$ contour interval and (b) resulting annual mean upper layer Sverdrup streamfunction transport, ψ with a 1-Sv contour interval.

4.1.1.4. *The fronts between 40°N and 50°N.* In the northern portion of the STG between 40°N and 50°N, from the Grand Banks to Europe, the Sverdrup flow characteristics generated by the 11 wind sets range from broad and diffuse to concentration into one or

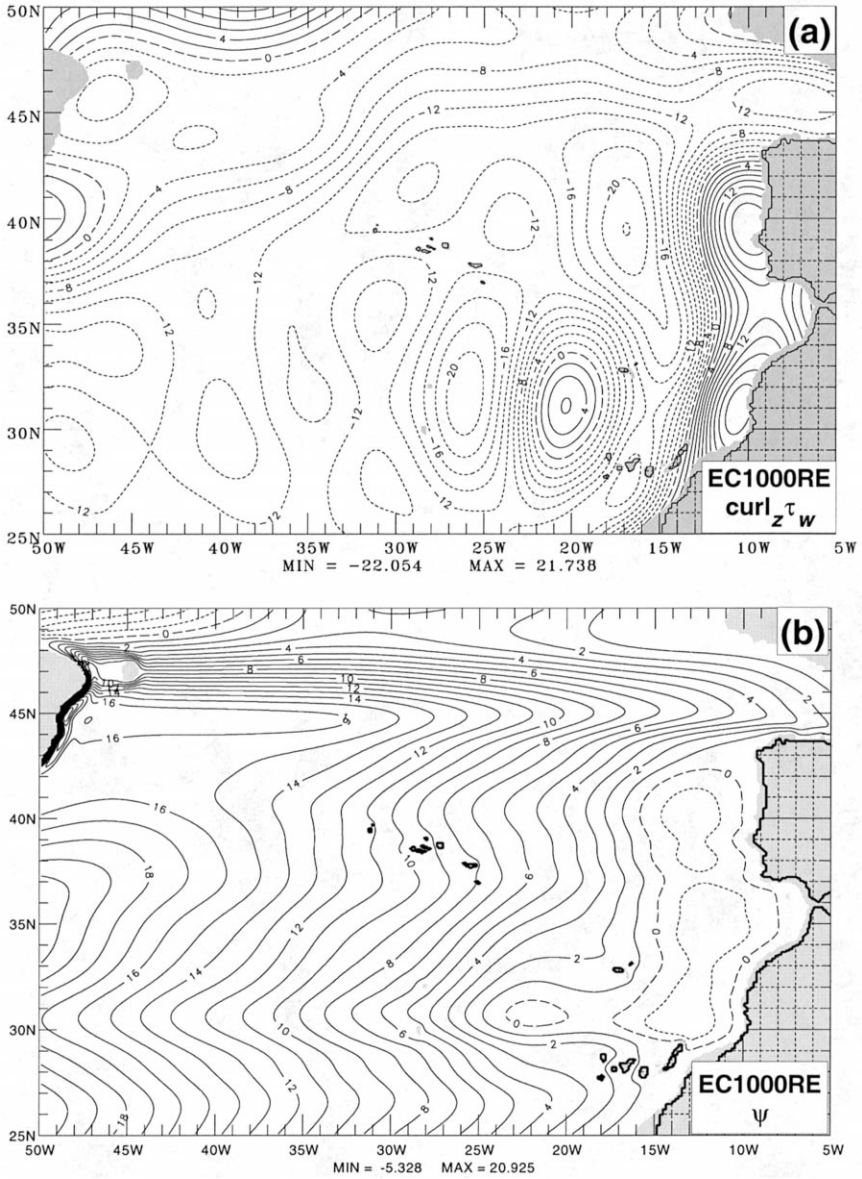


Fig. 6. Eastern STG region of the North Atlantic: (a) Annual mean wind stress curl from the ECMWF 1000 mb 1979–1993 re-analysis monthly mean wind stress climatology with a $2 \times 10^{-8} \text{ N m}^{-3}$ contour interval and (b) resulting annual mean upper layer Sverdrup streamfunction transport, ψ with a 1-Sv contour interval.

more fronts. The HRSM annual mean climatology exhibits relatively weak anti-cyclonic wind stress curl (Fig. 2a) across the basin in this latitude band. The very weak wind stress curl gradients (east–west and north–south), relative to most of the other wind sets,

result in broad eastward flow centered near 47°N (Fig. 4a) in the Sverdrup solution. The FNMOC surface stress climatology (Fig. 2j) produces a similar depiction of the Sverdrup transport streamfunction in this area, except that the axis of this flow is 2° further north (Fig. 4j).

An extreme contrast to the broad diffuse flow across this part of the basin in the HRSM and FNMOC results is seen in the 83–86EC1000 Sverdrup solution (Fig. 4f) with similar results in the remaining ECMWF simulations (Fig. 4e,g,h,i). In the annual mean wind stress curl of each of these data sets (Fig. 2e–i), there is a local anti-cyclonic maximum over the southern portion of the Bay of Biscay, which is located north of Spain and west of France (Fig. 3). This negative wind stress curl maximum north of Spain is near a local positive maxima near Portugal (Fig. 3) and another to its northwest near the southwest coast of Ireland where the latter has the greatest amplitude in the 83–86EC1000 wind data set (Fig. 2f) and is weakest in the 8596EC10M wind set (Fig. 2g). This wind stress curl pattern results in a band of eastward flow centered about 47°N that is concentrated within 3–5° of latitude. This front is maintained across the basin by the northwest–southeast gradient between the cyclonic wind stress curl of the subpolar low and the anti-cyclonic wind stress curl of the subtropical high. This gradient is stronger in the ECMWF wind stress climatologies (Fig. 2e–i) because the anti-cyclonic maximum north of the Azores and the local positive maximum south of Greenland at approximately 52°N are stronger than in the HRSM (Fig. 2a) and FNMOC (Fig. 2j) climatologies. Consequently, the northward flow in the subpolar gyre between the eastern edge of the western boundary current and 35°W (or the eastern boundary in the 83–86EC1000 simulation), occurs as far south as 48°N and the strong southward flow between 30°W and the eastern boundary occurs as far north as 45°N separated by a narrow band of strong eastward flow.

Another factor contributing to the stronger southward flow in the 44–48°N latitude band in all of the simulations is the additional anti-cyclonic wind stress curl integration distance near the eastern boundary which extends about 10° further east here due to the Bay of Biscay (Fig. 3). Also, there is a westward return flow immediately south of here along 44°N due to the local positive wind stress curl maximum just off the coast of Portugal. This feature is present in all the wind stress climatologies (Fig. 2a–k), but its amplitude and spatial extent varies among them.

4.1.2. *The subpolar gyre*

In the numerically computed Sverdrup solutions, the transport of the SPG ranges from 32 Sv in the EC10M simulation (Fig. 4g) to twice that much in the FNMOC case (Fig. 4j, Table 4) with the primary axis extending from the eastern edge of Greenland (Fig. 3) to the eastern boundary. This axis falls within the latitude band between 60°N and 62°N and coincides with the axis of the strongest positive wind stress curl in the subpolar North Atlantic. The ocean response in this region is a large, broad area of strong northward flow along this axis in all the simulations, with the strongest driven by FNMOC wind forcing. The boundary between the SPG and STG, as determined at the western boundary, lies consistently within the 48°N and 50°N latitude band with the southernmost occurrence found in the 83–86EC1000 solution and the northernmost in the FNMOC simulation.

In all but the HRSM (Fig. 4a) and HRUNSM (Fig. 4b) solutions, however, the strongest portion of the SPG in the Sverdrup transport streamfunction field is concentrated farther to the north (Fig. 4c–k). And with the winds from the atmospheric model–data assimilation systems (ECMWF, FNMOC, and NCEP; Fig. 4e–k), the southern boundary of the strongest part of the SPG is very zonal along 56°N. An exception to this is the FNMOC case (Fig. 4j), which exhibits a tilt of this boundary from 55°N in the west to 58°N in the east. The explanation for this is found by examining the wind stress curl pattern over the Atlantic north of 45°N. A consistent feature of the 11 climatological wind sets is the annual mean position of the zero wind stress curl line between the subtropical high and subpolar low (Fig. 2a–k). In the vicinity of 40°W, it dips as far south as approximately 47°N and curves northward to about 54–56°N at 30–25°W. The more northerly position east of 30°W results in southward flow south of about 55°N and northward flow north of this latitude in the eastern Atlantic. West of 30°W, in all but the HRSM and HRUNSM wind sets (Fig. 2a and b, respectively), there is a minimum in the positive wind stress curl south and/or southeast of Greenland, which separates strong positive curl to the north from a local wind stress curl maximum that occurs between approximately 55°N and the zero curl line at 47°N (Fig. 2c–k). This feature is more prominent in some of the wind sets than in others in terms of its amplitude and/or its east–west extent. In the UC and IH winds, it is quite weak compared to the atmospheric model-based wind sets. The ECMWF (Fig. 2e–i) and NCEP (Fig. 2k) climatologies produce a pronounced northward excursion of the NAC in the annual mean Sverdrup solution between approximately 50°W and 40°W northward to the latitude of the local minimum wind stress curl south of Greenland. The NAC then turns eastward and flows parallel to and north of the latitude of the northernmost anti-cyclonic wind stress curl east of 30°W as it feeds the Irminger Current (Fig. 4e–i,k). In the 83–86EC1000 simulation (Fig. 4f), this northward excursion meanders sharply to the west, then back to the east between 48°N and 53°N. This is due to reduced northward transport in this latitude band, which is required in order to balance the southward flow that develops between 34°W and the eastern boundary in response to the band of anti-cyclonic wind stress curl that is bounded by local positive wind stress curl maxima to the north and south. The effect of the UC, IH, and FNMOC winds on ψ is the same, albeit less dramatic. In the two HR-forced simulations, the eastward flow in the southern portion of the SPG is broad and diffuse with no meanders of the NAC whatsoever, due to the absence of the cyclonic wind stress curl minimum south of Greenland.

4.1.3. The northern tropical gyre

The NTG transport varies from 6 Sv in the UC simulation to 17 Sv in the EC1000RE case (Table 4). At the longitude of the Lesser Antilles (Fig. 1d), the boundary between the STG and the NTG to the south (Table 4) varies by more than 2° of latitude from 14.5°N between Martinique and St. Lucia Islands in the UC simulation (Fig. 4c) to 17°N between Antigua and Guadeloupe in the EC10M and EC10MRE simulations (Fig. 4g and i, respectively). In each of the Sverdrup solutions (Fig. 4a–k), the portion of the NTG that lies north of $\sim 11^\circ\text{N}$ extends from the tropical Atlantic into the southern Caribbean to the western boundary at Nicaragua. From there, the compensating western

boundary current flows southward then eastward along the Colombian and Venezuelan coasts. It exits the Caribbean through Grenada Passage and continues southeastward along the western boundary to about 4°N to close the NTG. The eastward Sverdrup flow through Grenada Passage and southeastward flow along the northeast coast of South America is opposite to the observed flow (Wilson and Johns, 1997). The Panama–Colombian gyre observed in the southwest Caribbean is part of the NTG, although, its extent across the southern Caribbean from the western boundary to approximately 65°W in most of the Sverdrup solutions presented here is unrealistically large. To explain these discrepancies, it is essential to consider the role of the global thermohaline circulation in this region, as discussed in Section 5.

4.2. Sverdrup flow within the IAS

The Sverdrup transports and transport pathways in the IAS region of the North Atlantic also depend on the wind set used to compute them. In addition, they are strongly influenced by the presence of the island chain that separates the Caribbean Sea from the North Atlantic Ocean as evidenced by the deflection of the Sverdrup transport streamfunction contours impinging on the Atlantic side of the Lesser and Greater Antilles (Fig. 4). Within the Caribbean Sea, the boundary between the STG and NTG forms the westward-flowing Caribbean Current. This extension of the NEC begins in the far eastern Caribbean where flow from both gyres enters through the passages of the Greater and Lesser Antilles. In the central portion of the Caribbean Sea, the Caribbean Current in the Sverdrup solution from each wind set intensifies in response to a strong wind stress curl dipole over the Caribbean (Fig. 2). Associated with this are a cyclonic gyre to the south of the Caribbean Current and an anti-cyclonic gyre to the north, which is complicated by Caribbean inflow through Mona and Windward Passages. Despite this inflow, the northern gyre is marked by eastward Sverdrup flow in the vicinity of Jamaica (Fig. 1c) in response to all of the wind sets (Fig. 4). Differences occur in the transport of the Caribbean Current and the anti-cyclonic and cyclonic circulations in the central Caribbean between the solutions due mainly to (1) differences in the strength of the STG and NTG, which in turn are due to differences in the wind stress curl fields over the STG and NTG regions of the Atlantic Ocean, and (2) differences in the amplitudes of the anti-cyclonic and cyclonic wind stress curl features over the central Caribbean.

All of the primary circulation features in the Gulf of Mexico are produced by each of the 11 wind stress climatologies, with the exception of FNMOC (Fig. 4j). However, as expected, the linear solution for the Loop Current clearly does not compare well with the observed mean position. This is due to the fact that the northward penetration of the Loop Current in linear simulations depends on a non-dimensional number which is analogous to a sidewall β Ekman number (Hurlburt and Thompson, 1982), which in turn depends on the eddy viscosity. Therefore, it is small compared to the northward penetration in a nonlinear simulation, which depends on the β -Rossby number and an associated length scale of $\sqrt{v/\beta}$. In the linear simulations, the Loop Current hugs the Campeche Bank and shows little northward penetration into the Gulf of Mexico. Instead, it bends westward along Campeche Bank until it separates from the boundary and continues due westward to the Mexican coast. It then returns toward the east and exits

through the Florida Straits. The width of this westward loop depends on the northernmost latitude of Campeche Bank, the southernmost latitude of the Florida shelf, and the eddy viscosity.

Even though each of the primary features of the Gulf of Mexico can be identified in each of the linear solutions, the amplitudes of these features vary significantly from simulation to simulation, with the ECMWF winds yielding the strongest Loop Current transport, cyclonic gyre in the Bay of Campeche and anti-cyclonic gyre in the northern Gulf (Fig. 4e–i). The Sverdrup transport feeding the Loop Current via Yucatan Channel (Table 6) varies from 14.5 Sv in the FNMOC wind-driven simulation to nearly 26 Sv in the IH simulation. Local wind forcing within the Gulf of Mexico also affects the penetration of the Loop Current in the linear solution. For example, the UC (Fig. 4c) and FNMOC (Fig. 4j) solutions have nearly the same transport through Yucatan Channel into the Gulf of Mexico (Table 6), but the westward penetration of the Loop Current is very different between the two. The westward penetration is stronger in the FNMOC case due to the weakly positive wind stress curl that occurs as far north as 27°N over a significant portion of the western Gulf. All of the other wind stress climatologies derived from atmospheric model products have anti-cyclonic wind stress curl as far south as 23°N in this area. Local wind forcing within the Gulf of Mexico also produces the anti-cyclonic gyre in the northern Gulf and the cyclonic gyre in the Bay of Campeche.

According to SR91, 13 Sv of the transport through the Florida Straits (Fig. 1c) is the thermohaline return flow from the South Atlantic. Schmitz et al. (1992) indicate that the remaining 17 Sv of the Florida Straits transport enters the Caribbean south of the Bahamas and is in Sverdrup balance with the winds east of 55–60°W. The latter determination was made based on Sverdrup transports in the ocean interior computed from the HR wind stress climatology by Roemmich and Wunsch (1985) along 24°N and from BU's wind stresses for the entire North Atlantic by Leetmaa and Bunker (1978). Using the numerically computed wind-driven Yucatan Channel transport (Table 6) as a more quantitative measure of the Sverdrup flow through the Caribbean Sea, the HRSM and HRUNSM wind sets nearly duplicate this result with a value of 19 Sv. A similar value is obtained using the EC10M, EC10MRE and NCEP wind stress climatologies. However, the amount of wind-driven flow through Yucatan Channel ranges from 14.5 Sv in the FNMOC simulation to 25.6 Sv in the IH simulation.

Note the difference, however, between the STG flow exiting the Caribbean Sea and the flow exiting the Florida Straits at 27°N in each of the linear wind-driven simulations (Table 6). The 27°N Florida Straits transport is comprised of Caribbean outflow entering the Florida Straits via the Gulf of Mexico plus additional Atlantic STG transport into the Florida Straits via Old Bahama and Northwest Providence Channels (Fig. 1c, Table 6). In the EC10M simulation, the numerically computed Sverdrup flow through these two passages is 4 and 5 Sv, respectively. When combined with the 17 Sv through the Caribbean, there is 26 Sv of wind-driven northward flow through the Florida Straits. With the addition of a 14-Sv MOC (consistent with SR91), the resulting 40 Sv is about 8 Sv greater than the observed Florida Straits transport of approximately 32 Sv between Florida and Grand Bahama Island (Larsen, 1992). This disagreement between the observed and linear wind-plus thermohaline-driven Florida Straits transport is generally symptomatic of all 11 simulations. The explanation for this discrepancy lies in the

Table 6

Sverdrup transports through the Florida Straits and passages of the Caribbean Sea and Bahamas calculated numerically by forcing a linear, $1/16^\circ$, 1.5-layer, hydrodynamic, reduced gravity version of NLOM for the Atlantic Ocean north of 30°S with 11 different wind stress data sets (Positive to the north and east)

Transport section	Location		Wind stress climatology											
	Latitude, $^\circ\text{N}$	Longitude, $^\circ\text{W}$	HRSM	HRUNSM	UC	IH	EC1000	83–86EC1000	EC10M	EC1000RE	EC10MRE	FNMOC	NCEP	
Florida Current at 27°N	27.0	80.7–78.6	26.0	24.5	23.8	38.7	36.0	38.8		25.6	6.6	27.4	19.4	23.6
NW Providence Channel	25.5–27.0	78.6	–5.1	–2.9	–7.4	–10.5	–8.0	–10.9		–5.0	–8.8	–6.3	–3.2	–5.2
Florida Current at 25.5°N	25.5	80.7–78.6	20.9	21.6	16.4	28.2	28.0	27.9		20.6	27.8	21.1	16.2	18.4
Old Bahama Channel	22.0–23.5	78.6	–2.0	–2.8	–1.5	–2.6	–5.4	–5.7		–3.8	–5.6	–4.3	–1.7	–2.6
Yucatan Channel	22.0	87.8–84.2	18.9	18.8	14.9	25.6	22.6	22.2		16.8	22.2	16.8	14.5	15.8
Windward Passage	18.5–20.3	74.4	–9.5	–9.4	–6.6	–11.1	–15.3	–14.7		–11.6	–13.2	–11.4	–6.6	–8.3
Mona Passage	18.5	68.4–67.0	–4.0	–3.8	–2.7	–5.2	–5.6	–3.9		–4.1	–5.5	–3.8	–3.3	–1.6
Anegada Passage	18.3	65.3–62.8	–1.2	–1.4	–0.9	–1.8	–0.3	–0.7		–0.2	–1.1	–0.3	–1.3	–0.8
Guadeloupe Passage,N	16.9–17.0	61.7	–0.6	–0.6	–0.6	–1.2	–0.6	–0.8		–0.5	–0.9	–0.6	–0.5	–0.6
Guadeloupe Passage,S	16.7–16.8	61.7	–0.8	–0.8	–0.7	–1.6	–0.8	–1.1		–0.6	–1.2	–0.8	–0.7	–0.8
Dominica Passage	15.7–15.8	61.5	–0.7	–0.7	–0.7	–1.2	–0.7	–1.1		–0.5	–0.9	–0.5	–0.6	–0.8
Martinique Passage	15.3	61.3–60.2	–2.5	–2.5	–2.5	–4.2	–2.8	–4.5		–1.6	–3.3	–1.5	–2.2	–2.9
St. Lucia Channel	14.0–14.5	61.0	–1.6	–1.4	–1.5	–2.6	–1.5	–2.3		–0.6	–1.1	–0.5	–1.6	–1.7
St. Vincent Passage	13.4–13.5	61.1–60.9	–0.8	–0.7	–0.6	–1.3	–0.4	–0.5		–0.2	–0.1	–0.2	–0.8	–0.7
Grenada Passage	11.0–12.0	61.7	2.8	2.5	1.9	4.6	5.4	7.4		3.1	5.1	2.8	3.1	2.4

difference between the observed and Sverdrup transport pathways in and around the Bahamas.

The observed northward transport at 26.5°N east of Abaco Island in the Bahamas is about 5 Sv in the upper ocean (Lee et al., 1996), while the linear wind-driven simulations show very little northward transport in this region (Fig. 4). Also, each simulation shows too much transport through Old Bahama plus Northwest Providence Channels in comparison to observational estimates totaling about 4 Sv (2 Sv through each) (Richardson and Finlen, 1967; Atkinson et al., 1995). However, if we take the total observed western boundary current transport in this region to be the sum of the Florida Straits transport at 27°N plus the transport east of Abaco at 27°N (similar to the approach of Roemmich and Wunsch, 1985 and Schmitz et al., 1992), we have the best observed measurement of western boundary current transport (37 Sv) in the North Atlantic. This is a valuable comparison for the linear simulations, when the 14-Sv upper ocean thermohaline component is added to the wind-driven transport. By this comparison, most of the wind products drive a linear oceanic response, which agrees to within about 10% of the observed western boundary current transport in this region. Exceptions are the IH wind stresses and the three ECMWF 1000 mb wind products, which drive transports that are much too high and the transport driven by the FNMOC surface stress product, which is too low by just over 10%. The unrealistically large transport associated with the IH wind stresses has been previously pointed out by Schmitz et al. (1992). Even though the observed circulation east of the Bahamas has a wind-driven component, the linear solutions indicate that higher order dynamics are required to explain northward flow in a western boundary current east of the Bahamas and to give more realistic (i.e., less) transport through Old Bahama and Northwest Providence Channels and, consequently, the Florida Straits at 27°N.

5. The impact of the global thermohaline circulation

In addition to the wind-forced features, the North Atlantic circulation has a significant buoyancy-driven component that is comprised of deep water formation in the far North Atlantic, southward-flowing NADW and an upper ocean return flow. This MOC is part of the global thermohaline circulation discussed by Gordon (1986), Broecker (1991), and Schmitz (1995). SR91 explained how 45% of the observed Florida Straits transport is comprised of the northward return flow waters by tracing their origin as far as the South Atlantic. Fratantoni et al. (1995, 2000) delineated the different pathways of the upper portion of the MOC through the tropical Atlantic. We can gain additional insight into the contribution of the global thermohaline circulation to the upper North Atlantic circulation by examining the impact of a linear version of the upper portion of the MOC, which is depicted as a Munk western boundary layer (Fig. 7a), on the Sverdrup/Munk solutions. This linear thermohaline solution was produced by the same 1/16° linear model that produced the wind-driven Sverdrup/Munk solutions, except that it was forced only by a 14-Sv mass flux imposed at ports in the northern and southern boundaries (Fig. 1a, Table 2).

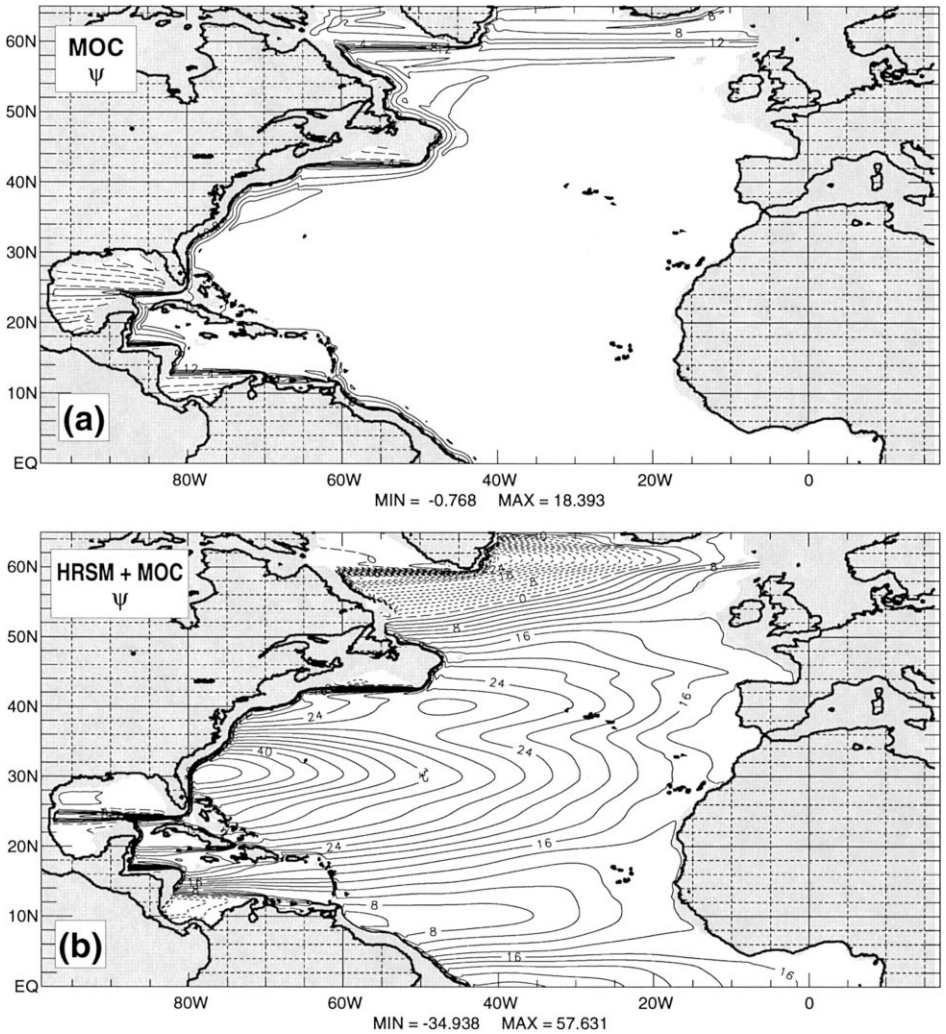


Fig. 7. Annual mean upper layer transport streamfunction from the $1/16^\circ$, 1.5-layer, linear NRL layered model (NLOM) of the Atlantic Ocean north of 30°S forced only by the upper portion of a 14-Sv MOC via ports in the northern and southern model boundaries. (b) as in (a) after addition of the linear solution produced by HRSM wind forcing only (Fig. 4a). The contour interval is 2 Sv.

5.1. Impact of the MOC on the Gulf Stream system

Using the observed upper ocean transport of 5 Sv east of Abaco Island (Lee et al., 1996) plus the observed transport of 32 Sv through the Florida Straits (Larsen, 1992) as a measure of the observed western boundary current transport in the North Atlantic, we can compare the total of 37 Sv with the linear wind- plus thermohaline-driven simulation transports in this region, as Lee et al. (1996) did for the HR winds. When the

14 Sv MOC (SR91) is added, the western boundary current transport here is increased and most of the linear solutions agree with the observed transport to within about 10% except for the IH and ECMWF 1000 mb simulations. The same is true of highly nonlinear simulations with $1/32^\circ$ resolution forced by HRSM and UC along with the MOC (Hurlburt and Hogan, 2000, this issue). The total northward western boundary current transport at 27°N is explained by Sverdrup dynamics plus the known thermohaline-driven component of the western boundary current. The distribution of this northward flow on either side of Abaco Island, Bahamas differs between the linear and nonlinear solutions, with the latter being more realistic.

Between Cape Hatteras and the Grand Banks, the linear upper ocean branch of the MOC (Fig. 7a) follows the same pathway as the more northerly of the two Gulf Stream pathways in the linear wind-driven solution (Fig. 4a). Addition of the two solutions results in augmentation of the transport in the northern branch of the linear Gulf Stream solution by 14 Sv (Fig. 7b). The linear wind-driven Gulf Stream transport at Cape Hatteras also increases when the linear MOC is added, but the sum of these two solutions is much less than the observed value of 63 Sv (Richardson and Knauss, 1971). This is an indication that additional dynamics are necessary to explain the observed value. Hurlburt and Hogan (2000, this issue) show that nonlinearity plays an important role in the observed Gulf Stream transport at Cape Hatteras and that a much more realistic Gulf Stream pathway between Cape Hatteras and the Grand Banks is achieved compared to the two-branch linear Gulf Stream solution. They point out that the $\sim 60\%$ nonlinear augmentation of the western boundary current transport at Cape Hatteras is due to the nonlinear re-circulation gyre on the south side of the Gulf Stream. Some of the linear solutions (HRSM, HRUNSM, UC, IH, and FNMOC) also show a small wind-driven increase in the western boundary transport north of 27°N (Fig. 4).

5.2. Impact of the MOC on the SPG circulation

The western portion of the STG/SPG gyre boundary ($\psi = 0$) is moved approximately 4° northward from $\sim 49\text{--}50^\circ\text{N}$ (Fig. 4a) to $\sim 53\text{--}54^\circ\text{N}$ (Fig. 7b) when the linear thermohaline solution is added as a Munk western boundary layer. The linear wind-driven western boundary current transport in the NAC source region off the Grand Banks (Dietrich et al., 1975) is 13 Sv in the HRSM simulation (Fig. 4a). When the linear upper MOC solution is added, the value increases to 27 Sv (Fig. 7b).

If we define the linear pathway of the NAC such that it follows along the southern side of the STG/SPG boundary, we see that adding the linear MOC to the linear wind-driven flow also gives a more northerly pathway of the NAC east of $25\text{--}30^\circ\text{W}$. In this region of the SPG, the wind- plus thermohaline-driven NAC more closely follows the observed position along $\sim 60^\circ\text{N}$ (Krauss, 1986) and flows into the Nordic sea region (Fig. 7b). Although vertical mixing is not included in the linear simulations, it also plays an important role in the circulation within the SPG.

5.3. Impact of the MOC on the low-latitude circulation

In the wind-driven Sverdrup/Munk solutions, the NTG lies partly in the Caribbean Sea (Fig. 4a) and, as discussed in Section 4.1.3, does not compare well to the observed

large-scale circulation in the southern Caribbean. Wind forcing is not solely responsible for the observed large-scale features in this region. Addition of the linear MOC (Fig. 7a) alters the linear wind-driven circulation pattern in the following ways (Fig. 7b). First, there is a reversal of the east- and southeastward-flowing western boundary current along the northern coast of South America. A Guyana Current flows northwestward along the South American coast from about 5°N to the southern passages of the Lesser Antilles (Fig. 1d). A westward boundary current flows along the Venezuela coast as far as the Guajira Peninsula of Colombia (Fig. 1b). From there, it flows zonally across the southwestern Caribbean to the Nicaraguan coast. Second, the eastward extension of the Panama–Colombian gyre retreats to a more realistic position and is detached from the NTG as observed.

Within the eastern Caribbean Sea, the linear thermohaline-driven western boundary current flowing westward along Venezuela does not immediately join the linear wind-driven Caribbean Current. However, west of the Guajira Peninsula, it does join and augment the Caribbean Current transport. Farther downstream, it also augments the transport of the Yucatan and Loop Currents. The strength of the Loop Current penetration into the Gulf of Mexico (westward in a linear solution, as previously explained) is also enhanced when the global thermohaline circulation is added.

6. Summary, conclusions and recommendations

The large-scale circulation of the North Atlantic, as it relates to the wind stress curl, has been investigated by analyzing the Sverdrup transport streamfunction fields produced by a $1/16^\circ$ linear numerical ocean model forced by 11 different wind stress climatologies. Even though each wind set produces the observed basic large-scale features of the North Atlantic surface circulation, the importance of carefully selecting a wind stress climatology for the computation of Sverdrup transports is emphasized by the substantial differences in the flow patterns and transport magnitudes of several circulation features. In addition to comparisons of the wind-driven characteristics of these features, the impact of the thermohaline circulation on the Sverdrup solution was shown for the Gulf Stream, NAC, tropical Atlantic, and IAS regions. The numerical modeling approach to this analysis has revealed more details of the Sverdrup flow within the major gyre systems of the North Atlantic than shown in previous studies (e.g., Leetmaa et al., 1977; Leetmaa and Bunker, 1978; Roemmich and Wunsch, 1985; Schmitz et al., 1992; Fratantoni et al., 2000). The detailed representation of the coastline and islands in the high-resolution ocean model has also facilitated understanding the influence of the complicated geometry of the North Atlantic on the Sverdrup flow. Because the linear solutions include only the lowest order dynamics of the ocean, they provide a baseline comparison of ocean model response to different wind forcing products. They also provide a benchmark for other simulations which have added features such as nonlinearity, bottom topography, multiple vertical modes, flow instabilities, thermal forcing and vertical mixing.

In each of the Sverdrup/Munk solutions, the Gulf Stream consists of an unrealistic split Gulf Stream pathway. One branch flows due east from Cape Hatteras. A second branch overshoots the observed point of separation from the coast at Cape Hatteras and

continues to flow adjacent to the model boundary all the way to approximately 43°N . There, it finally separates from the boundary and flows eastward to the Grand Banks. The unrealistic northern branch is the northward western boundary current required to balance the mass constraint of southward Sverdrup flow east of $\sim 50^{\circ}\text{W}$. This northern “overshoot” Gulf Stream pathway is augmented by the addition of a linear version of the upper thermohaline component of the North Atlantic circulation. An $O(1)$ change from linearity is required to achieve a single realistic nonlinear pathway between Cape Hatteras and the Grand Banks in a numerical ocean model. Many nonlinear, eddy-resolving basin-scale models of the North Atlantic Ocean (e.g., Bryan et al., 1995; Dengg et al., 1996; DYNAMO Group, 1997; Ezer and Mellor, 2000; Hurlburt and Hogan, 2000 (their $1/8^{\circ}$ results), this issue) also have a two-branch depiction of the mean Gulf Stream pathway similar to the Sverdrup solution.

Using Sverdrup dynamics, three mechanisms that may contribute to the observed C-shape of the subtropical gyre were identified. The first involves two areas of positive wind stress curl in the eastern STG at approximately 30°N and positive wind stress curl over the Gulf of Cadiz. The second mechanism is dual zonal bands of relatively strong negative wind stress curl separated by a weaker band in the subtropical high. The third mechanism is a local maximum of anti-cyclonic wind stress curl along approximately 24°N to 26°N east of the Bahamas to about 65°W . If this wind stress curl feature is present in the wind stress climatology and the Sverdrup transport streamfunction exhibits a C-shape in the western STG, then the southern portion of the C-shape is enhanced in this region due to the increased southward transport in response to this curl feature.

The Azores Current is present in all but one of the linear simulations with transports of 1–2 Sv, indicating that a portion of the observed transport, albeit less than 20%, is explained by Sverdrup dynamics. There is a southward recirculation in the Azores Current, which feeds into an approximately westward flow along 31 – 32°N in the Sverdrup solutions that have a C-shaped STG, which includes all but the HR-forced simulations. This recirculation and zonal return to the west is in agreement with observations (Tychensky et al., 1996).

The strongest portion of the SPG is concentrated to the north in all but the HRSM and HRUNSM solutions. South of Greenland, a local minimum in the wind stress curl bisects the area of positive wind stress curl west of 30°W and causes a northward excursion of the NAC. The NAC then turns east and flows parallel to and north of the latitude of northernmost anti-cyclonic wind stress curl east of 30°W as it feeds the Irminger Current. There is a noticeable impact by the thermohaline flow on the wind-driven circulation of the SPG. The western portion of the STG/SPG boundary is $\sim 4^{\circ}$ farther north after the addition of the linear thermohaline circulation and the western boundary current transport in the NAC source region off the Grand Banks is augmented. Also, the linear wind- plus thermohaline-driven NAC pathway in the eastern SPG is farther to the north and more realistic than in the linear wind-driven simulations.

In each wind-driven simulation, the northern portion of the NTG extends from the Atlantic basin into the IAS to the western boundary of the Caribbean Sea. The gyre-closing boundary current flows southward then eastward, exiting the IAS through Grenada Passage and continuing southeastward along the northeast coast of Brazil. From

the Guajira Peninsula of Colombia, this eastward and then southeastward flow within the NTG is opposite to the observed direction of the mean flow in this region. Addition of the linear MOC alters the wind-driven pattern such that this flow is reversed.

The strength and the distribution of the flow feeding the Caribbean Current is dependent on the basin-scale wind forcing and the geometry of the Greater and Lesser Antilles. Once this flow enters the Caribbean Sea, the transport increases in response to a wind stress curl dipole over the central Caribbean. Within the Gulf of Mexico, each primary circulation feature is produced, although with varying amplitudes, by each of the wind sets, except FNMOC. Local wind forcing over the Gulf of Mexico is responsible for the anti-cyclonic circulation in the northern Gulf and the cyclonic circulation in the Bay of Campeche. It can also affect the strength of the westward penetration of the Loop Current in the linear solution. The linear thermohaline-driven solution significantly impacts the wind-driven solutions within the Caribbean Sea and Gulf of Mexico. West of the Guajira Peninsula of Colombia, it augments the Caribbean Current transport and farther downstream, it augments the transport of the Yucatan and Loop Currents, as well as the Florida Straits transport. In the southwest Caribbean Sea, the Panama–Colombian gyre retreats to a more realistic east–west extent. And, within the Gulf of Mexico, the Loop Current penetration is enhanced.

Each of the wind-driven linear simulations produces a wind-driven Florida Straits transport that is too high compared to the long-term mean observed value of 32 Sv (Larsen, 1992) minus the 13–14 Sv thermohaline contribution (SR91). However, there is an observed northward transport of 5 Sv in the upper ocean just east of Abaco Island in the Bahamas where the linear simulations show very little transport. Using the sum of the observed northward transport through the Florida Straits and east of Abaco Island as a measure of the observed western boundary current transport, most of the linear wind-plus thermohaline-driven solutions agree with the observed transport to within about 10%, the exceptions being the IH and the three ECMWF 1000 mb simulations which are ~ 35–45% too high. Comparison of the linear solution transports downstream at Cape Hatteras with observed values and strongly nonlinear $1/32^\circ$ simulations indicates that nonlinearity plays an important role in the observed Gulf Stream transport at Cape Hatteras (Hurlburt and Hogan, 2000, this issue).

Three criteria are used to evaluate each of the 11 wind stress climatologies (Table 3) for driving large-scale nonlinear models of the North Atlantic Ocean, particularly in relation to simulation of the Gulf Stream. Each criterion involves a well-known feature of the North Atlantic circulation related to the Gulf Stream. (1) The observed western boundary current transport at $26.5\text{--}27^\circ\text{N}$ (Florida Straits plus upper ocean transport along Abaco Island) is well-established and often compared to the Sverdrup interior (taking the thermohaline contribution into account), this paper included. In the first evaluation step, the linear wind- plus thermohaline-driven western boundary current transport produced by each wind set is compared to the observed value. (2) If criterion (1) is satisfied, we look for relatively strong western boundary current transport near Cape Hatteras to facilitate formation of strong inertial flow where the Gulf Stream separates from the coast. (3) Since we know that the Gulf Stream separates from the western boundary at Cape Hatteras and flows east–northeastward to the Grand Banks, we look for a relatively weak overshoot path in the linear wind-driven solution.

Using these three criteria and the linear simulations, the HRSM and UC wind stress climatologies perform the best overall followed by the EC10M and the NCEP re-analysis wind stress climatologies. However, both of the latter have relatively weak linear transports near Cape Hatteras. The IH wind stresses and ECMWF 1000 mb wind products (EC1000, 83–86EC1000, and EC1000RE) are too strong and are the only wind sets that are clearly inappropriate to use as is. The ECMWF wind products (EC10M and EC10MRE included) do produce the most realistic southern linear Gulf Stream pathways with the greatest eastward extension produced by the shorter time frame 83–86EC1000 winds. The ECMWF 1000 mb winds might be useful for driving a numerical ocean model, if they were first adjusted to the standard uniform height of 10 m. EC10MRE satisfies criterion (1), but produces the weakest linear transport near Cape Hatteras of all the products, about 10% weaker than the next weakest products, EC10M and the NCEP re-analysis. The FNMOC surface stresses give better results than the IH wind stresses and EC1000 mb wind products, with regard to the three criteria. However, they produce a weak Florida Straits transport and they have the strongest overshoot pathway of the 11 wind sets. The unsmoothed Hellerman–Rosenstein wind stresses (HRUNSM) produce an unobserved current separating from the western boundary at $\sim 31^\circ\text{N}$, when interpolated to a fine resolution model grid (not seen in Sverdrup flow calculations performed on the native grid using centered differences). The HRSM and UC wind sets are both capable of giving a reasonable Gulf Stream depiction in a nonlinear model (Hurlburt and Hogan, 2000, this issue). They also show little difference in the large-scale C-shape of the STG despite some large differences between the corresponding linear solutions, a reason we did not use this as criterion in evaluating the wind sets. At least for the mean position of the Gulf Stream, the EC10M and the NCEP re-analysis wind stresses also show promise for North Atlantic Ocean modelers wanting to use an interannual time series of winds from an atmospheric model. If one assumes that the strength of the linear overshoot Gulf Stream pathway is not important in strongly nonlinear simulations, then the FNMOC surface stresses should also work well for Gulf Stream simulation, but with weak transport through the Florida Straits.

Acknowledgements

This work is a contribution to the Global and Basin-Scale Ocean Prediction System projects under program element 62435N, to the Data Assimilation and Model Evaluation Experiments-North Atlantic Basin (DAMEE-NAB) project, and to the Dynamics of Low-Latitude Western Boundary Currents project under program element 61153N, all projects at NRL sponsored by the Office of Naval Research. The ocean model simulations were performed on the Cray Y-MP 8/8128, the Cray C90/161024, the Cray T90, the SGI Power Challenge Array, and the SGI Origin 2000 at the Naval Oceanographic Office, Stennis Space Center, Mississippi using grants of computer time under the Department of Defense High Performance Computing initiative. Thanks are extended to Alan J. Wallcraft (NRL) for his contribution in developing the ocean model, E. Joseph Metzger (NRL) for acquiring and processing the wind forcing fields derived from the atmospheric model analyses, and Thomas Mitzka (IFM) for the Isemer–Hasse climatology.

References

- Atkinson, L.P., Berger, T., Hamilton, P., Waddell, E., Leaman, K., Lee, T.N., 1995. Current meter observations in the Old Bahama Channel. *J. Geophys. Res.* 100, 8555–8560.
- Böning, C.W., Döscher, R., Isemer, H.J., 1991a. Monthly mean wind stress and Sverdrup transports in the North Atlantic: a comparison of the Hellerman–Rosenstein and Isemer–Hasse Climatologies. *J. Phys. Oceanogr.* 21, 221–235.
- Böning, C.W., Döscher, R., Budich, R.G., 1991b. Seasonal transport variation in the western subtropical North Atlantic: experiments with an eddy-resolving model. *J. Phys. Oceanogr.* 21, 1271–1289.
- Broecker, W.S., 1991. The great ocean conveyor. *Oceanography* 4, 79–89.
- Bryan, F.O., Böning, C.W., Holland, W.R., 1995. On the midlatitude circulation in a high-resolution model of the North Atlantic. *J. Phys. Oceanogr.* 25, 289–305.
- Bunker, A.F., 1976. Computations of surface energy flux and annual air–sea interaction cycles of the North Atlantic Ocean. *Mon. Weather Rev.* 104, 1122–1140.
- Chao, Y., Gangopadhyay, A., Bryan, F.O., Holland, W.R., 1996. Modeling the Gulf Stream system: how far from reality? *Geophys. Res. Lett.* 23, 3155–3158.
- da Silva, A.M., Young, C.C., Levitus, S., 1994a. Algorithms and procedures. Atlas of Surface Marine Data 1994. Vol. 1, NOAA Atlas NESDIS 6, U.S. Department of Commerce, NOAA, NESDIS, 83 pp.
- da Silva, A.M., Young, C.C., Levitus, S., 1994b. Anomalies of heat and momentum fluxes. Atlas of Surface Marine Data 1994. Vol. 3, NOAA Atlas NESDIS 8, U.S. Department of Commerce, NOAA, NESDIS, 413 pp.
- Dengg, J., Beckmann, A., Gerdes, R., 1996. The Gulf Stream separation problem. In: Krauss, W. (Ed.), *The warmwatersphere of the North Atlantic Ocean*. Gebr. Borntraeger, Berlin, pp. 253–290.
- Dietrich, G., Kalle, K., Krauss, W., Siedler, G., 1975. *General Oceanography, An Introduction*. 2nd edn. Wiley, New York, 626 pp.
- Dukowicz, J.K., Smith, R.D., 1994. Implicit free-surface method for the Bryan–Cox–Semtner ocean model. *J. Geophys. Res.* 99, 7991–8014.
- DYNAMO Group, 1997. DYNAMO, Dynamics of North Atlantic Models: Simulation and Assimilation with High Resolution Models. Rep. 294, Institut Für Meereskunde an der Universität Kiel, Kiel, Germany, 333 pp.
- European Centre for Medium-Range Weather Forecasts (ECMWF), 1994. The description of the ECMWF/WCRP level III — A global atmospheric data archive. In: *Meteorological Bulletin M3.2*. ECMWF, Reading, Berkshire, UK, 72 pp.
- European Centre for Medium-Range Weather Forecasts (ECMWF), 1995. User guide to ECMWF products. In: *Meteorological Bulletin M3.2*. ECMWF, Reading, Berkshire, UK, 71 pp.
- Ezer, T., Mellor, G.L., 2000. Sensitivity studies with the Sigma coordinate Princeton Ocean Model. *Dyn. Atmos. Oceans* 32, 185–208.
- Fratantoni, D.M., Johns, W.E., Townsend, T.L., 1995. Rings of the North Brazil Current: their structure and behavior inferred from observations and a numerical simulation. *J. Geophys. Res.* 100, 10633–10654.
- Fratantoni, D.M., Johns, W.E., Townsend, T.L., Hurlburt, H.E., 2000. Low-latitude circulation and mass transport pathways in a model of the tropical Atlantic Ocean. *J. Phys. Oceanogr.* 30, (in press).
- Gibson, J.K., Kallberg, P., Uppala, S., Hernandez, A., Nomura, A., Serrano, E., 1997. ECMWF Re-Analysis Project Report Series: 1. ERA Description. ECMWF, Reading, Berkshire, UK, 71 pp.
- Godfrey, J.S., 1989. A Sverdrup Model of the depth-integrated flow for the ocean allowing for island circulations. *Geophys. Astrophys. Fluid Dyn.* 45, 89–112.
- Gordon, A.L., 1986. Interocean exchange of thermocline water. *J. Geophys. Res.* 91, 5037–5046.
- Heburn, G.W., 1994. The dynamics of the seasonal variability of the western Mediterranean circulation. In: LaViolette, P.E. (Ed.), *Seasonal and Interannual Variability of the Western Mediterranean Sea*, Coastal Estuarine Stud. 46, AGU, Washington, DC, pp. 249–285.
- Hellerman, S., 1967. An updated estimate of the wind stress in the World Ocean. *Mon. Weather Rev.* 95, 607–626, (with corrected tables in vol. 96, 62–74).
- Hellerman, S., 1968. Correction. *Mon. Weather Rev.* 96, 63–74.
- Hellerman, S., Rosenstein, M., 1983. Normal monthly wind stress over the world ocean with error estimates. *J. Phys. Oceanogr.* 13, 1093–1104.

- Hogan, T.F., Rosmond, T.E., 1991. The description of the Navy Operational Global Atmospheric Prediction System's spectral forecast model. *Mon. Weather Rev.* 119, 1786–1815.
- Hurlburt, H.E., Hogan, P.J., 2000. Impact of $1/8^\circ$ to $1/64^\circ$ resolution on Gulf Stream model–data comparisons in basin-scale subtropical Atlantic Ocean models. *Dyn. Atmos. Oceans*, this issue.
- Hurlburt, H.E., Thompson, J.D., 1980. A numerical study of Loop Current intrusions and eddy shedding. *J. Phys. Oceanogr.* 10, 1611–1651.
- Hurlburt, H.E., Thompson, J.D., 1982. The dynamics of the Loop Current and shed eddies in a numerical model of the Gulf of Mexico. In: Nihoul, J.C.J. (Ed.), *Hydrodynamics of Semi-Enclosed Seas*. Elsevier, Amsterdam, pp. 243–297.
- Hurlburt, H.E., Wallcraft, A.J., Schmitz, W.J. Jr., Hogan, P.J., Metzger, E.J., 1996. Dynamics of the Kuroshio/Oyashio current system using eddy-resolving models of the North Pacific Ocean. *J. Geophys. Res.* 101, 941–976.
- Isemer, H.J., Hasse, L., 1985. The Bunker climate atlas of the North Atlantic Ocean. In: *Observations vol. 1* Springer-Verlag, Heidelberg, 218 pp.
- Isemer, H.J., Hasse, L., 1987. The Bunker climate atlas of the North Atlantic Ocean. In: *Air–Sea Interactions vol. 2* Springer-Verlag, Heidelberg, 256 pp.
- Kalnay, E., Kanamitsu, M., Kistler, R., Collins, W., Deaven, D., Gandin, L., Iredell, M., Saha, S., White, G., Woollen, J., Zhu, Y., Chelliah, M., Ebisuzaki, W., Higgins, W., Janowiak, J., Mo, K.C., Ropelewski, C., Wang, J., Leetmaa, A., Reynolds, R., Jenne, R., Joseph, D., 1996. The NCEP/NCAR 40-Year Reanalysis Project. *Bull. Am. Meteorol. Soc.* 77, 437–471.
- Kaufeld, L., 1981. The development of a new Beaufort equivalent scale. *Meteorol. Rundsch.* 34, 17–23.
- Klein, B., Siedler, G., 1989. On the origin of the Azores Current. *J. Geophys. Res.* 94, 6159–6168.
- Krauss, W., 1986. The North Atlantic Current. *J. Geophys. Res.* 91, 5061–5074.
- Larsen, J.C., 1992. Transport and heat flux of the Florida Current at 27°N derived from cross-stream voltages and profiling data: theory and observations. *Philos. Trans. R. Soc. London, Ser. A* 338, 169–236.
- Lee, T.N., Johns, W., Schott, F., Zantopp, R., 1990. Western boundary current structure and variability east of Abaco, Bahamas at 26.5°N . *J. Phys. Oceanogr.* 20, 446–466.
- Lee, T.N., Johns, W.E., Zantopp, R.J., Fillenbaum, E.R., 1996. Moored observations of western boundary current variability and thermohaline circulation at 26.5°N in the subtropical North Atlantic. *J. Phys. Oceanogr.* 26, 962–983.
- Leetmaa, A., Bunker, A.F., 1978. Updated charts of the mean annual wind stress, convergences in the Ekman layers, and Sverdrup transports in the North Atlantic. *J. Mar. Res.* 36, 311–322.
- Leetmaa, A., Niiler, P., Stommel, H., 1977. Does the Sverdrup relation account for the mid-Atlantic circulation?. *J. Mar. Res.* 35, 1–10.
- Levitus, S., 1982. *Climatological Atlas of the World Ocean*. U.S. Government Printing Office, Washington, DC, NOAA Prof. Paper 13, 173 pp.
- Mann, C.R., 1967. The termination of the Gulf Stream and the beginning of the North Atlantic Current. *Deep-Sea Res.* 14, 337–359.
- Mauritzen, C., 1993. A study of the large-scale circulation and water mass formation in the nordic seas and Arctic Ocean, PhD Dissertation, Massachusetts Institute of Technology and Woods Hole Oceanographic Institution, 221 pp.
- McManus, A.P., Townsend, T.L., Metzger, E.J., 1997. Creation and Modification of $1/8^\circ$ and $1/16^\circ$ Subtropical Gyre Atlantic Topographies. Naval Research Laboratory, Stennis Space Center, MS, NRL/FR/7323-95-9626, 23 pp.
- Mesinger, F., Arakawa, A., 1976. *Numerical Methods Used in Atmospheric Models*. World Meteorol. Org., Geneva, Switzerland, GARP Publ. Ser., No. 17, 64 pp.
- Metzger, E.J., Hurlburt, H.E., 1996. Coupled dynamics of the South China Sea, the Sulu Sea and the Pacific Ocean. *J. Geophys. Res.* 101, 12331–12352.
- Metzger, E.J., Hurlburt, H.E., Kindle, J.C., Sirkes, Z., Pringle, J., 1992. Hindcasting of wind-driven anomalies using a reduced gravity global ocean model. *Mar. Technol. Soc. J.* 26 (2), 23–32.
- Munk, W.H., 1950. On the wind-driven ocean circulation. *J. Meteorol.* 7, 79–93.
- Myers, P.G., Haines, K., Josey, S., 1998. On the importance of the choice of wind stress forcing to the modeling of the Mediterranean Sea circulation. *J. Geophys. Res.* 103, 15729–15749.

- National Oceanic and Atmospheric Administration (NOAA), 1986. ETOPO5 digital relief of the surface of the earth. In: Data Announcement 86-MGG-07. National Geophysical Data Center, Boulder, CO.
- Richardson, W.S., Finlen, J.R., 1967. The transport of Northwest Providence Channel. *Deep-Sea Res.* 14, 361–367.
- Richardson, P.L., Knauss, J.A., 1971. Gulf Stream and western boundary undercurrent observations at Cape Hatteras. *Deep-Sea Res.* 18, 1089–1109.
- Rienecker, M.M., Atlas, R., Schubert, S.D., Willett, C.S., 1996. A comparison of surface wind products over the North Pacific Ocean. *J. Geophys. Res.* 101, 1011–1023.
- Roemmich, D., Wunsch, C., 1985. Two transatlantic sections: meridional circulation and heat flux in the subtropical North Atlantic Ocean. *Deep-Sea Res.* 32, 619–664.
- Schmitz, W.J., Jr., 1995. On the interbasin-scale thermohaline circulation. *Rev. Geophys.* 33, 151–173.
- Schmitz, W.J., Jr., 1996. Some global features/North Atlantic circulation. On the World Ocean Circulation. Vol. I, Woods Hole Oceanographic Institution Technical Report WHOI-96-03, 141 pp.
- Schmitz, W.J., Jr., McCartney, M.S., 1993. On the North Atlantic circulation. *Rev. Geophys.* 31 (1), 29–49.
- Schmitz, W.J., Jr., Richardson, P.L., 1991. On the sources of the Florida Current. *Deep-Sea Res.* 38, 379–409, (Suppl.).
- Schmitz, W.J., Jr., Thompson, J.D., Luyten, J.R., 1992. The Sverdrup circulation for the Atlantic along 24°N. *J. Geophys. Res.* 97, 7251–7256.
- Shriver, J.F., Hurlburt, H.E., 1997. The contribution of the global thermohaline circulation to the Pacific to Indian Ocean throughflow via Indonesia. *J. Geophys. Res.* 102, 5491–5511.
- Stommel, H., 1948. The westward intensification of wind-driven currents. *Trans. Am. Geophys. Union* 29, 202–206.
- Stommel, H., Niiler, P., Anati, D., 1978. Dynamic topography and recirculation of the North Atlantic. *J. Mar. Res.* 36, 449–468.
- Stramma, L., 1984. Geostrophic transport in the warm water sphere of the eastern subtropical North Atlantic. *J. Mar. Res.* 42, 537–558.
- Sverdrup, H.U., 1947. Wind-driven currents in a baroclinic ocean: with application to the equatorial currents of the eastern Pacific. *Proc. Natl. Acad. Sci. U. S. A.* 33, 318–326.
- Tychensky, A., Le Traon, P.-Y., Hernandez, F., Jourdan, D., Canceill, P., 1996. Structure and temporal evolution of the Azores Front during the SEMAPHORE-93 Experiment. *EOS, Trans. Am. Geophys. Union* 77 (46), F345, supplement.
- Vukovich, F.M., 1995. An updated evaluation of the Loop Current's eddy-shedding frequency. *J. Geophys. Res.* 100, 8655–8659.
- Wallcraft, A.J., 1991. The Navy Layered Ocean Model Users Guide. Naval Research Laboratory, Stennis Space Center, MS, NOARL Rep. 35, 21 pp.
- Wallcraft, A.J., Moore, D.R., 1997. The NRL layered ocean model. *Parallel Comput.* 23, 2227–2242.
- Wilson, W.D., Johns, W.E., 1997. Velocity structure and transport in the Windward Islands Passages. *Deep-Sea Res.* 44, 487–520.
- Woodruff, S.D., Slutz, R.J., Jenne, R.L., Steurer, P.M., 1987. A comprehensive ocean-atmosphere data set. *Bull. Am. Meteorol. Soc.* 68, 1239–1250.
- World Meteorological Organization (WMO), 1970. Reports on marine scientific affairs. Rep. No. 3. The Beaufort scale of wind force. WMO, 22 pp., Geneva, Switzerland.
- Wunsch, C., Roemmich, D., 1985. Is the North Atlantic in Sverdrup balance? *J. Phys. Oceanogr.* 15, 1876–1880.